The role of Mg in the crystallisation of monohydrocalcite.

Juan Diego Rodriguez-Blanco[1,2], Samuel Shaw[1,3], Pieter Bots[1,3], Teresa Roncal-Herrero[1], and Liane G. Benning[1,*]

[1]School of Earth and Environment. University of Leeds. Leeds LS2 9JT. United Kingdom.
[2]Now at the Nano Science Center, University of Copenhagen. 2100 Copenhagen, Denmark.
[3]School of Earth, Atmospheric and Environmental Sciences, The University of Manchester, Oxford Road, Manchester, M13 9PL.
* corresponding author: L.G.Benning@leeds.ac.uk

ABSTRACT

Monohydrocalcite is a member of the carbonate family which forms in Mg-rich environments at a wide range of Mg/Ca ratios ($Mg^{2+}_{aq}/Ca^{2+}_{aq} \geq 0.17 < 65$). Although found in modern sedimentary deposits and as a product of biomineralization, there is a lack of information about its formation mechanisms and about the role of Mg during its crystallization. In this work we have quantitatively assessed the mechanism of crystallization of monohydrocalcite through in situ synchrotron-based small and wide angle X-ray scattering (SAXS/WAXS) and off-line spectroscopic, microscopic and wet chemical analyses. Monohydrocalcite crystallizes via a 4-stage process beginning with highly supersaturated solutions from which a Mg-bearing, amorphous calcium carbonate (ACC) precursor precipitates. This precursor crystallizes to monohydrocalcite via a nucleation-controlled reaction in stage two, while in stage three it is further aged through Ostwald-ripening at a rate of 1.8±0.1 nm/$h^{1/2}$. In stage four, a secondary Ostwald ripening process (66.3±4.3 nm/$h^{1/2}$) coincides with the release of Mg from the monohydrocalcite structure and the concomitant formation of minor hydromagnesite. Our data reveal that monohydrocalcite can accommodate significant amounts of Mg in its structure (χ_{MgCO3}=0.26) and that its Mg content and dehydration temperature are directly proportional to the saturation index for monohydrocalcite (SI_{MHC}) immediately after mixing the stock solutions. However, its crystallite and particle size are inversely proportional to these parameters. At high

supersaturations (SI_{MHC}=3.89) nanometer-sized single crystals of monohydrocalcite form, while at low values (SI_{MHC}=2.43) the process leads to low-angle branching spherulites. Many carbonates produced during biomineralization form at similar conditions to most synthetic monohydrocalcites, and thus we hypothesize that some calcite or aragonite deposits found in the geologic record that have formed at high Mg/Ca ratios could be secondary in origin and may have originally formed via a metastable monohydrocalcite intermediate.

Keywords: monohydrocalcite, carbonates, magnesium, synchrotron, SAXS, WAXS, scattering.

1. INTRODUCTION

A variety of calcium carbonate minerals are stable at Earth surface conditions. These include the common polymorphs calcite, vaterite and aragonite, and the less common and hydrated phases monohydrocalcite ($CaCO_3 \cdot H_2O$) and ikaite ($CaCO_3 \cdot 6H_2O$). Monohydrocalcite forms in a variety of modern natural environments including saline spring waters (Ito, 1993), marine polar systems (e.g., Antarctic lakes, or Ikka Fjord, Greenland; Bird et al., 1991; Dahl and Buchardt, 2006), basaltic caves (Broughton, 1972; Onac, 2000; Léveillé et al., 2000), cold/humid mine galleries and lacustrine deposits. Representative of the latter environment is for example, the oldest known monohydrocalcite, 800 ka. (Solotchina et al. (2009), that was found in deep sediments at Lake Hovsgol, NW Mongolia. Other lacustrine examples include Lake Kivu in Africa, or Lake Fellmongery and Lake Butler in S. Australia (Stoffers and Fischbeck, 1974 and Taylor, 1975). Monohydrocalcite is usually found in association with other carbonates like Mg-calcite, aragonite, Ca-rich dolomite ($CaMg(CO_3)_2$) or Mg carbonates like hydromagnesite ($Mg_5(CO_3)_4(OH)_2 \cdot 4H_2O$) and nesquehonite ($MgCO_3 \cdot 3H_2O$) (Fischbeck and Mueller, 1971; Broughton, 1972; Nishiyama et al., 2013). Monohydrocalcite is also formed as a product of biomineralization by certain molluscs (Lowenstam, 1981), flatworms (calcareous corpuscles of Platyhelminthes; Señorale-Pose et al., 2008), vertebrates (otoliths; Carlström, 1963), guinea pigs (bladder stones; Skinner et al., 1977) or is even found as a decay product in Saguaro cacti (Garvie, 2003, 2006). It has also been described associated with algae (Taylor, 1975) or halo bacilli

(Rivadeneyra et al., 2004). However, despite its occurrence in a wide variety of systems little is known about the mechanism and kinetics of its formation pathway.

At Earth surface temperatures and pressures, monohydrocalcite is thermodynamically unstable relative to anhydrous calcite and aragonite. In the presence of a Mg-free aqueous fluid it will slowly (>2 days at 100 °C, several days/weeks at ambient temperature) transform to calcite (Stoffers and Fischbeck 1974; Taylor, 1975). Yet, even minor concentrations of aqueous magnesium will lead to its transformation to aragonite over 25 days at ambient temperatures (Brooks et al., 1950; Kamiya et al., 1977; Dahl and Buchardt, 2006; Munemoto and Fukushi, 2008; Fukushi et al., 2011). This effect is believed to be due to the inhibiting effect of Mg^{2+} on calcite crystallization (Chen et al., 2004; Mucci and Morse, 1983, Davis et al., 2000; Bots et al., 2011). The instability of monohydrocalcite with respect to calcite and aragonite explains the relatively low abundance of this phase within modern environmental systems and the geological record.

The mechanism of monohydrocalcite crystallisation in many systems is unknown, but some studies indicate that it can form from an amorphous precursor (Kamiya et al., 1977; Loste et al., 2003; Fukushi et al., 2011; Nishiyama et al., 2013). Such a crystallization pathway has been shown to be common for many Ca-Mg carbonates (e.g., vaterite, aragonite, dolomite; Bots et al., 2012; Rodriguez-Blanco et al., 2012; Sand et al., 2012; Rodriguez-Blanco et al., 2013; Ihli et al., 2012), and other carbonate and phosphate systems (Roncal-Herrero et al., 2009; Roncal-Herrero et al., 2011; Vallina et al., 2013), but this amorphous to crystalline transition is not ubiquitous (Van Driessche et al., 2012). In the carbonate system, these studies have shown that the transformation of the amorphous calcium carbonate (ACC) precursor to stable crystalline phases (i.e., vaterite, dolomite) occurs via a nucleation dominated (spherulitic) growth mechanism. Despite its presence in a variety of natural settings and biominerals, a quantitative evaluation of the kinetics and mechanisms of monohydrocalcite formation from an amorphous precursor is lacking.

Monohydrocalcite has a hexagonal structure with space group $P3_112$ and an atomic structure consisting of irregular 8-folded Ca-O polyhedra, with a central Ca^{2+} ion surrounded by carbonate groups and water molecules (Effenberger, 1981; Neumann and Epple, 2007; Swainson, 2008). The presence of the water makes its structure more open and less dense compared to anhydrous $CaCO_3$ (e.g., calcite or aragonite). Interestingly, monohydrocalcite is described as a pure 'calcium' carbonate phase in mineralogical databases, but a number of studies have shown that Mg is ubiquitous in all synthetic and natural monohydrocalcite samples (Mg/Ca= ~ 0.01-0.53; Hull and Turnbull, 1973; Taylor, 1975; Neumann and Epple,

2007; Nebel et al., 2008; Fukushi et al., 2011; Nishiyama et al., 2013). The Mg content of monohydrocalcite is likely to be linked to the overall fluid chemistry and in particular to the Mg contents of the fluid in which it forms. In both natural and most synthetic monohydrocalcites the presence of high concentrations of Mg relative to Ca in the precipitating solution ($Mg^{2+}_{aq}/Ca^{2+}_{aq} \geq 0.17 < 65$) is a prerequisite for its formation (e.g., Munemoto and Fukushi, 2008; Neumann and Epple, 2007; Last et al., 2010; Kimura and Koga, 2011). Recently, Nishiyama et al (2013) have also shown that the crystallinity and particle size of synthetic monohydrocalcite decrease with Mg content. This clearly shows that Mg is a key component in monohydrocalcite, and must be present in the fluids in which it crystallizes. However, the exact mechanisms by which Mg controls the formation and stability of monohydrocalcite are unknown.

This study aims to determine the mechanism of monohydrocalcite crystallisation in solution via an ACC precursor. We evaluate the role of Mg during this process and test the hypothesis that a nucleation-dominated process controls the formation of monohydrocalcite from the Mg-containing precursor ACC. This has been done through a series of experiments where the nucleation and crystallization of monohydrocalcite from Mg doped-ACC was followed in situ and in real time with synchrotron-based X-ray scattering combined with microscopic and wet chemical characterization of the solids and solutions throughout the reaction. Our results demonstrate that the formation of monohydrocalcite takes place via a 4-stage process that starts with the precipitation of an Mg-rich ACC precursor. This precursor crystallizes in stage two to monohydrocalcite through a nucleation-controlled dissolution-reprecipitation reaction. In stage three Ostwald-ripening dominates, while in stage four, a secondary monohydrocalcite crystallization, also through Ostwald ripening, occurs concomitantly with the loss of some of its structural Mg. We also show that, depending on the aqueous Mg/Ca ratio and supersaturation, monohydrocalcite can accommodate large amounts of Mg in its structure (up to ~25% Ca replaced by Mg) and that the aqueous chemistry of the starting solution controls the crystallite size, unit-cell dimensions and particle size/shape of the forming monohydrocalcite. Based on these findings we discuss the implications of this monohydrocalcite crystallization pathway, on its occurrence in various natural settings and as a biomineral.

2. EXPERIMENTAL

Experiments were carried out at 21 °C by rapid addition (under constant and vigorous stirring) of a $CaCl_2/MgCl_2$ solution (700 mM $CaCl_2$; 300 mM $MgCl_2$; Ca/Mg ratio of 7/3) to a 1000mM Na_2CO_3 solution to achieve a $(Ca+Mg)/CO_3$ ratio of 1/1. In all cases immediately upon mixing a white gel precipitated. The crystallization of this white gel was followed on-line using in situ and time resolved small and wide angle X-ray Scattering (SAXS/WAXS) on beamline I22 (Diamond Light Source Ltd., UK). Solutions were mixed using a stopped-flow apparatus (Bio-Logic, Paris, France) and the resulting white suspensions were continuously circulated with a peristaltic pump through a capillary cell in line with the synchrotron beam. Simultaneous SAXS (RAPID detector; Marchal et al., 2009) and WAXS (HOTWAXS detector; Bateman et al., 2007) patterns were collected over 12 hours at 1 min/frame. The time resolved scattering patterns were detector-response corrected, and background subtracted using a scattering pattern from the starting Na_2CO_3 solution. Individual WAXS patterns were fit using XFIT (Cheary and Coelho, 1992) and the areas under the Bragg peaks normalized to values from 0 to 1 to express the degree of reactions (α) as a function of time (Rodriguez-Blanco et al., 2011). Crystallite size was calculated from the Bragg peak full-width half-maximum (FWHM) using the Scherrer equation (Scherrer, 1918) and the unit cell parameters were determined with TOPAS (Coelho, 2006), using the Swainson (2008) model for the monohydrocalcite structure.

The variations in the scattering peak position in the SAXS patterns were used to derive the changes in the particle sizes of the solids throughout the experiments via the expression:

$$d = 2\pi/q \quad [1]$$

where d (nm) is particle diameter and q (nm^{-1}) is the scattering vector (de Moor et al, 1999; de Moor et al, 1999b). These particle size results were also cross-validated by whole SAXS pattern fitting using GNOM (Svergun, 1992).

Experiments equivalent to the online SAXS/WAXS experiments (i.e., 1000mM Na_2CO_3 solution mixed with a 700 mM $CaCl_2$ and 300 mM $MgCl_2$ solution) were performed to follow the reaction process via time-dependent solid characterization and solution analyses. At specific time steps aliquots of the reacting suspension were removed and immediately vacuum filtered (0.2 μm polycarbonate membranes). The resulting solids were washed with water and isopropanol following Rodriguez-Blanco et al (2008). An aliquot of each solid sample was dissolved in 0.1 M HCl and analysed together with the corresponding

solution samples for aqueous Ca and Mg concentrations ($[Ca^{2+}_{aq}]$ and $[Mg^{2+}_{aq}]$) using ion chromatography (Dionex LC 220) following Bots et al (2011). Throughout all experiments the pH was recorded at a 10 second time resolution using an Orion pH meter and WinWedge v3.4.1 software (TAL technologies) with a precision of 0.001. Finally, the total carbonate concentration in solution was determine by assuming that all Ca and Mg precipitated formed Ca/Mg carbonate, therefore the moles of Ca + Mg removed form solution must equal the total moles of carbonate removed. The total carbonate was then calculated from the difference between the initial concentration and the amount removed at each time point. From these solution data the saturation indexes (SI) with respect to different Ca and Mg-bearing carbonates were calculated using PHREEQC (Parkhurst, 1995) and are presented in Table 1. This was done using the Pitzer activity coefficient models (Pitzer, 1979) and two solubility products, $K_{sp(MHC)}$, for monohydrocalcite ($10^{-7.60}$; Hull and Turnbull, 1973) and ($10^{-7.05}$; Krajl and Brečević, 1995). The saturation index of monohydrocalcite is defined as:

$$SI_{MHC} = \log \frac{a_{Ca^{2+}} \times a_{CO_3^{2}}}{K_{sp(MHC)}} \qquad [2]$$

To determine the effect of initial supersaturation (i.e. saturation index of the aqueous solution for monohydrocalcite immediately after mixing the stock solutions) on the crystallization reaction, experiments were also performed following the same procedure but starting at different initial supersaturations with respect to monohydrocalcite, yet keeping a 1/1 (Ca+Mg)/CO_3 ratio (Table 2) in all cases. Using the $[Ca^{2+}_{aq}]$ and $[Mg^{2+}_{aq}]$ concentrations obtained from the analyses of the dissolved solids, the molar fraction of $MgCO_3$ in each solid sample, X_{MgCO3}, was calculated following:

$$_{MgCO_3} = \frac{M_{MgCO_3}}{M_{MgCO_3} + M_{CaCO_3}} \qquad [3]$$

where M_{MgCO3} and M_{CaCO3} correspond to the molar concentration of $MgCO_3$ and $CaCO_3$, respectively.

The mineralogy of the solids from off-line experiments was characterized by powder X-ray diffraction (PXRD) using a Bruker D8 X-ray Diffractometer (CuKα1, 5-90° two theta,

198 0.001°/step; 0.1 or 1 sec/step). The PXRD patterns were also used to derive the crystallite
199 size using the Scherrer equation (Scherrer, 1918). All samples were imaged by high-
200 resolution transmission electron microscopy (HR-TEM; Philips CM200 field emission gun
201 TEM equipped with a Gatan Imaging Filter, GIF-200 and a Gatan camera for selected area
202 electron diffraction, SAED, pattern collection) or scanning electron microscopy (SEM; LEO
203 1530 Gemini). Finally, the water content of the samples was determined using
204 thermogravimetric analyses (TGA, Mettler Toledo, 25-800 °C in air, 10°C/min). The total
205 water content for the initial white precipitate was calculated from the difference in weight
206 between 25 and 550°C in accordance with the method of Radha et al. (2012) for determining
207 the water content of ACC. For crystalline samples the difference in weight between 100 and
208 550°C was used, in accordance with the method of Hull and Turnbull (1973) for determining
209 the water content of monohydrocalcite.
210
211
212 **3. RESULTS AND DISCUSSION**
213
214 Our data revealed that over the 12 hours of our experiments monohydrocalcite formed
215 through a multi-stage crystallisation pathway. The first stage of the reaction was
216 characterized by the formation of a Mg-bearing amorphous calcium carbonate phase. In stage
217 two, this amorphous phase crystallised to nanoparticulate monohydrocalcite. The rate of
218 crystallization slowed considerably during stage three, coincident with only minor changes
219 in the solution composition (e.g., pH). Finally, in the fourth stage of the reaction secondary
220 growth of the nanoparticulate monohydrocalcite was observed. This was accompanied by the
221 simultaneous decrease in [Mg^{2+}_{aq}] and the formation of minor amounts of hydromagnesite
222 ($Mg_5(CO_3)_4(OH)_2{\cdot}4H_2O$). Each of these four stages is described in detail below:
223 In **Stage I** of the reaction a white gel precipitated immediately upon solution mixing.
224 The PXRD patterns of this gel (Fig. 1a, lower pattern) showed no Bragg peaks and only three
225 humps located at 2θ (λ=1.54 Å) 17, 31 and 45°, indicating the solid is poorly-ordered. These
226 three broad humps (asterisks in Fig. 1a), are located at the same positions as those observed
227 for Mg-free amorphous calcium carbonate (ACC; Rodriguez-Blanco et al., 2008). Based on
228 the chemical analyses of this amorphous phase (Table 1, 0.83 hour sample) and the TGA
229 results, the formula for this compound was determined to be $Ca_{0.74}Mg_{0.26}CO_3{\cdot}1.18H_2O$. In
230 line with previous studies where the incorporation of Mg into ACC has been quantified

(Nebel and Epple, 2008; Wang et al., 2009; Rodriguez-Blanco et al., 2012), we will term this poorly-ordered phase, Mg-ACC, following the notation of Günther et al (2005). Throughout this first stage, Mg-ACC was the only solid phase present. In both the on-line and off-line experiments and regardless of conditions, the Mg-ACC started to crystallize after approximately 50 minutes to 1 hour, initiating **Stage II**. During this stage the background intensity in the PXRD patterns decreased with time, and Bragg peaks for monohydrocalcite formed, grew and sharpened (Fig. 1a). The on-line time resolved WAXS data (Fig. 1b) shows the simultaneous growth of the monohydrocalcite (110), (111), (300) and (301) peaks, after ~ 1 hour. The whole reaction is clearly illustrated when the change in area for a specific Bragg peak, expressed as the degree of reactions (α), is plotted as a function of time (Fig. 2). Stage II of the reaction lasted for about 1 hour and was characterized by the rapid increase in monohydrocalcite peak area. After the fast growth in stage II, a much slower growth phase, between ~ 2 and 8 hours followed (**stage III**). During this stage, only minor changes in Bragg peak intensities / areas were observed (Fig. 1b and 2). The final stage of the reaction -**stage IV**- started after about 8.3 hours. During this stage a secondary growth in the monohydrocalcite Bragg peak areas was observed. This growth phase lasted about 2-3 hours and the peak areas reaching a stable maximum after ~ 11 hours. This same evolution was observed for all other monohydrocalcite Bragg peaks. An PXRD examination of off-line experimental solids sampled during stage IV revealed the presence of a second, but minor phase of hydromagnesite (ICDD PDF 01-070-1177; Fig. S1). Quantitative X-ray refinement with TOPAS (Coelho, 2006) determined that its abundance was ~4.5%. The on-line time resolved WAXS patterns (Fig. 3) also revealed small hydromagnesite (110) and (011) Bragg peaks that began to grow at the onset of stage IV, in parallel with the second stage of monohydrocalcite crystallization.

Analysis of the SAXS data (Fig. 4) indicates that the Mg-ACC that formed in stage I consisted of particles with a diameter of between 40 and 60 nm in size, a size that remained constant throughout this first stage. This is consistent with particle sizes derived from the TEM imaging of the Mg-ACC particles, which indicted an average diameter of ~ 40 nm (n=100; Fig. 5a; Table 1). However, the Mg-ACC particle diameters varied between 15 and 210 nm revealing a high degree of polydispersity. The corresponding SAED patterns revealed only diffuse rings for the Mg-ACC, confirming its poorly-ordered nature (Fig. 5d). During stage II, a distinct scattering peak appeared in the SAXS patterns (arrows in Fig. 4a) indicating that the crystals formed in the experiment were relatively monodispersed. The position of the scattering peak in the time resolved SAXS patterns moved towards lower q

with time indicting particle growth (Fig. 4a). From the position of this peak and using equation [1] the particle size of the monohydrocalcite crystals was determined (Fig. 4b). At the beginning of stage II, when the first Bragg peaks for monohydrocalcite appeared in the WAXS data (Fig. 1b and Fig. 2), the corresponding SAXS data revealed an average diameter of ~9 nm for the newly forming monohydrocalcite crystals. During the rest of stages II and III these monohydrocalcite nanocrystals grew only slightly and very slowly reaching a maximum diameter of ~15 nm after 8 hours. This same trend in average particles sizes was confirmed (open symbols in Fig. 4b) through selected full pattern evaluation with GNOM (Svergun, 1992). TEM microphotographs of the monohydrocalcite that formed in stage II and persisted throughout stage III (Fig. 5b) revealed that the monohydrocalcite consisted of nanocrystals, which exhibited sub-spherical to slightly elongated morphologies. Their average dimensions were 28±7 (L) x 20±5 (W) nm, with the minimum size being around 14x10 nm (n=100). The corresponding SAED pattern showed diffraction rings with only poorly developed spots (Fig. 5e), evidencing the presence of very small but crystalline nanocrystals. At the onset of stage IV, and simultaneously with the secondary growth in Bragg peak areas for monohydrocalcite, the SAXS data also revealed a steady increase in the monohydrocalcite nanocrystal diameters, which reached a maximum of ~45 nm at the end of the reaction. Photomicrographs of a sample obtained after 10 hr (stage IV; Fig. 5c) showed euhedral or subhedral single monohydrocalcite crystals with sizes of 77±20 (L) x 47±10 (W) nm. Again large variations in dimensions were observed, with the largest and smallest crystals being 155x80 and 40x30 nm (n=100). SAED pattern from these crystals exhibited clearly defined spots within the diffraction rings (Fig. 5f). HR-TEM images of the sample taken from the end of stage IV (Fig. 5c, white arrow) revealed the presence of hydromagnesite as a minor phase consisting of ~100x5 nm platy crystals, confirming the WAXS and PXRD observations (Fig. 3 and Fig. S1).

Evaluating the corresponding WAXS patterns for the Scherrer crystallite size (Fig. 2) showed a reasonable agreement with the particle size determined from the SAXS and TEM data, and also confirmed that the forming monohydrocalcite crystals were anisotropic. For example, based on the Bragg peak (110) the data reveals that the monohydrocalcite crystals formed during stage II had a crystallite size of ~15 nm, increasing to ~ 20 nm during stage III, which is in agreement with the particle sizes derived from the SAXS and TEM data. Once stage IV of the crystallization was initiated, the monohydrocalcite nanocrystallite size steadily increased to > 80 nm, which is almost double the average particle size from SAXS,

but closer to that derived from the TEM data. However, although this general trend was the same in all other Bragg peaks, the crystallite sizes in all stages were dramatically different between the different Bragg peaks. For example, the final crystallite size from the (141) peak at the end of stage 3 was 16 nm, half that of the (110) peak, and at the end of the reaction it only reached a value of 28 nm (Fig. 2), almost three times smaller than the final crystallite size from the (110) peak, indicating a clear anisotropic growth of the monohydrocalcite nanocrystals. This is consistent with the elongated particle morphology observed by TEM.

Analysis of the WAXS data also revealed changes in unit cell dimensions during the formation of monohydrocalcite (Fig. 6). Once formed, the unit cell volume (721.6 $Å^3$) remained virtually constant during stages II-III with a slight decrease during stage IV ($\Delta V \approx -0.2$ $Å^3$; Fig. 6a). However, more substantive changes were observed in the a and c axis dimensions (Fig. 6b and c, respectively). Their evolution mirrored each other, with the a-axis decreasing and the c-axis increasing in length ($\Delta c = -\Delta a \approx 0.02$ Å). These changes were small during stages II and III, but became more significant during the secondary monohydrocalcite crystallization (stage IV).

The changes in solution and solid phase chemistry during the formation and crystallisation of monohydrocalcite showed a clear link between the evolution of pH, $[Ca^{2+}_{aq}]$, $[Mg^{2+}_{aq}]$ and molar fraction of Mg in the solids (Fig. 7) over the four stage of the reaction. The reaction started with a pH of 11.60 (the pH of the initial Na_2CO_3 solution), which upon mixing with the Ca/Mg solution rapidly dropped to 9.17. During stage I the pH increased slightly reaching a value of 9.24, while the formation of monohydrocalcite in stage II did not change the pH. In stage III only a small decrease in pH to a value of 9.16 was evident. However, at the end of stage III and during stage IV the pH dropped dramatically to 8.65. The $[Ca^{2+}_{aq}]$ was 1.25 mM during stage I and decreased to ≈ 0.6 mM by stage III. It then decreased further reaching a concentration < 0.1 mM at the end of stage IV (Fig. 7). $[Mg^{2+}_{aq}]$ was 28 mM during stages I and II, but increased by ~ 20 % to 35 mM during stage III. During stage IV it decreased by 40% to 13 mM. These changes in $[Mg^{2+}_{aq}]$ were mirrored throughout the whole reaction by the change in χ_{MgCO3} in the solids (Fig. 7). Furthermore, the timing of these changes in aqueous composition were all coupled with the increase in monohydrocalcite particle size (Fig. 4 and 5) and formation of hydromagnesite (Fig. 3).

From the χ_{MgCO3} values and the TGA results, the formula of the stage II monohydrocalcite was derived to be $Ca_{0.74}Mg_{0.26}CO_3 \cdot 0.99H_2O$. However, although the total χ_{MgCO3} increased during stage IV (Fig. 7), this does not represent the Mg in monohydrocalcite

but primarily the contribution from the minor (~ 4.5%) hydromagnesite ($Mg_5(CO_3)_4(OH)_2$ $4H_2O$). Using the quantitative XRD results and the composition of the final solid obtained from chemical analysis (χ_{MgCO3} = 0.26, Table 1) we calculated that the molar fraction of Mg in monohydrocalcite at the end of stage IV was only ~ 0.065 moles, which is a 75% decrease compared to the Mg content of the stage II monohydrocalcite (0.26 moles). The remaining Mg was transferred into the newly formed hydromagnesite.

One last line of evidence that supports the observations above is the evolution of the saturation states during the reaction. PHREEQC modelling of the solution during the reaction showed that immediately after the precipitation of Mg-ACC upon mixing, the aqueous solution was supersaturated with respect to both monohydrocalcite and hydromagnesite (Fig. 8) and that the SI for both phases varied little during stages I to III ($SI_{MHC} \approx 0.5$; $SI_{HMgS} \approx 6$). The biggest change in both SI occurred at the onset of stage IV, where SI_{MHC} became undersaturated ($\approx$ -0.85) while SI_{HMgS} dropped to $\approx$ 0.2. This change in SI was concomitant with the removal of Mg from solution and the associated drop in pH, due to the formation of hydromagnesite. There are however, two factors that need to be taken into account when SI_{MHC} is calculated. Firstly, two solubility products for monohydrocalcite are available in the literature: $10^{-7.60}$ (Hull and Turnbull, 1973), and $10^{-7.05}$ (Krajl and Brečević, 1995) and this results in a ~0.55 difference in the calculated SI_{MHC} (Fig. 8). Secondly, the total ionic strength in our experiments was high ($\leq$1 M) and thus even an error of 1% in the ionic strength of the starting solution could also result in variations up to ~0.5 units in the calculated SI_{MHC}.

3.1. Stability of the precursor Mg-ACC and the mechanism of monohydrocalcite nucleation and growth

The formation of monohydrocalcite proceeded, in all our experiments, through a poorly-ordered Mg-ACC precursor, which precipitated from solutions with an initial $[Ca^{2+}_{aq}]$:$[Mg^{2+}_{aq}]$ of 7:3. The resulting phase was considerably more stable (crystallization started at ~50 minutes) compared to pure ACC (no Mg; crystallization started <2 minutes; Ogino et al., 1987; Rodriguez-Blanco et al., 2011; Rodriguez-Blanco et al., 2012, Bots et al., 2012), or Mg-ACC formed in a solution with $[Ca^{2+}_{aq}]$:$[Mg^{2+}_{aq}]$ of 9 to 1 (crystallized to calcite within ~ 14 minutes; Rodriguez-Blanco et al., 2012). However, the Mg-ACC in the current study was less stable than Mg-ACC produced from solutions where 50% of the

364 calcium was replaced with magnesium (i.e., $[Ca^{2+}_{aq}]:[Mg^{2+}_{aq}]$ = 1:1), which did not
365 crystallize at ambient temperatures even after longer reaction times (>1 day; Rodriguez-
366 Blanco et al., 2013). The increasing stability of ACC with increasing Mg contents is not
367 unexpected, and confirms both abiotic (Rodriguez-Blanco et al., 2011; Rodriguez-Blanco et
368 al., 2013; Ajikumar et al., 2005) and biotic (Politi et al,. 2010; Loste et al., 2003; Raz et al.,
369 2003) data that demonstrate the importance of Mg in stabilizing amorphous precursors and
370 delaying crystallization. The most likely cause of these effects is the high dehydration energy
371 of the Mg-aquo ion compared to the Ca ion (di Tommaso and de Leeuw, 2010). Hydrated and
372 poorly-ordered ACC is less thermodynamically stable than the dehydrated and more-ordered
373 ACC. This dehydration and local ordering in the amorphous precursor precedes its
374 crystallization (Radha et al., 2010; Bots et al., 2012). Hydrated Mg located within the
375 nanoporous structure of ACC (Goodwin et al., 2010) would retard its dehydration and
376 breakdown, slowing its transformation to crystalline phases.
377 In stage I and prior to the formation of monohydrocalcite, the pH increased by a small
378 amount (0.07 units) (Fig. 7), which likely corresponds to the release of OH^- due to the onset
379 of Mg-ACC dissolution. Kojima et al (1993) showed that ACC incorporates minor amounts
380 of OH^- ions into its structure when it forms at a basic starting pH. The Mg-ACC in our on-
381 line experiment started forming at a pH of 11.5 (the pH of the carbonate starting solution;
382 Fig. 7) and thus minor OH^- in our Mg-ACC is not unexpected. Its dissolution would release
383 OH^- ions, thus explaining the slight pH increase following:
384
385 $$Ca(OH)_{2x}(CO_3)_{1-x}\cdot yH_2O \rightarrow Ca_{1-x}(CO_3)_{1-x} + Ca^{2+}_{x,\,aq} + (OH)^-_{2x,\,aq} + yH_2O \quad [4]$$
386
387 The first monohydrocalcite crystals formed during stage II were significantly smaller
388 than the initial Mg-ACC nanoparticles (Fig. 4b), yet once monohydrocalcite started forming,
389 its diameter remained virtually constant throughout stage II and III. Analysis of the WAXS
390 data shows that the amount of monohydrocalcite crystallising increased at a constant rate
391 throughout stage II of the reaction (Fig. 2). However, this increase was not due to particle
392 growth (Fig. 4b) and we suggest that the formation of monohydrocalcite during stage II
393 proceeds via the nucleation of new crystalline solids, i.e., via a nucleation-controlled reaction.
394 The constant rate of monohydrocalcite crystallization with time (i.e., linear increase in the
395 amount of monohydrocalcite) during most of stage II indicates a zeroth order reaction, and a
396 constant rate of nucleation. Furthermore, the pH remained virtually constant during stage II,

indicating a constant dissolution of Mg-ACC coupled with the constant nucleation of monohydrocalcite. Taking all this into account, we propose that the transformation form Mg-ACC to monohydrocalcite occurs via a simultaneous dissolution of Mg-ACC and nucleation of monohydrocalcite at a constant rate. Nucleation controlled growth has been shown for several other crystalline carbonate phases formed from amorphous Ca-Mg carbonates (e.g., vaterite and proto-dolomite; Bots et al., 2012; Rodriguez-Blanco et al., 2013). These studies suggested that the large difference in solubility between the amorphous precursor and the crystalline phases as well as the high supersaturations with respect to all crystalline phases, promotes nucleation. This nucleation process will continue until all of the amorphous precursor has been consumed, leading to a constant nucleation rate.

Stage IV of the reaction is key to understanding the effect of Mg on the formation of monohydrocalcite. The SAXS data (Fig. 4b) shows a dramatic increase in particle size. During stage IV, this increase can be fitted to a straight line when plotted as a function of $t^{1/2}$, indicating a surface-controlled Ostwald-ripening mechanism (Wagner, 1961; Tobler et al., 2009). TEM images and both WAXS and PXRD data confirm that larger and better developed monohydrocalcite crystals formed during this stage of the reaction, supporting the Ostwald-ripening mechanism. The photomicrographs of monohydrocalcites from stages III and IV (Fig. 5 b and c) show an unambiguous increase in the nanocrystal sizes and a corresponding change in the SAED patterns from rings with faint spots to discrete spots, indicting an increase in particle size.

Ostwald ripening usually occurs during the later stages of crystallisation reactions and involves particle growth without the formation of new material (Wagner, 1961). All nanoparticles formed in stages III are undoubtedly crystalline, but some of them are too small (<10 nm) to produce a significant amount of diffraction. Therefore scattering from these crystal is observed in the background of the PXRD/WAXS patterns during stages II and III (e.g. Fig. 1 after 1 hour of reaction). This behaviour is similar to that observed for ultra-small iron oxides crystallites which are too small to diffract singly (Machala et al., 2007; Ahmed et al., 2010). The intensity of the background in the XRD/WAXS patterns decreased during stages III and IV, while the Bragg peaks increased in intensity and became sharper. These changes in background and Bragg peak intensity are not due to the formation of more monohydrocalcite, but reflect the growth of the monohydrocalcite nanoparticles to a size where they diffract strongly, due to the Ostwald ripening process. The linear fits to the particle growth data with the surface-controlled growth model Fig. 4b show different rates

(slopes) for the Ostwald-ripening process during stages III (slow; 1.8±0.1 nm/$h^{1/2}$) and IV (fast; 66.3±4.3 nm/$h^{1/2}$).

The rapid change in monohydrocalcite ripening rate is coincident with the formation of hydromagnesite; its formation lead to the fast removal of Mg from solution and triggered the rapid increase in monohydrocalcite growth rate. We suggest that structural Mg from monohydrocalcite during the ripening process was released into the solution leading to the observed increase in [Mg^{2+}_{aq}] during stage III (Fig. 7). This ultimately drove the monohydrocalcite composition toward a pure $CaCO_3 \cdot H_2O$ end-member. The high concentration of Mg in solution during stage II suppressed the ripening rate, and produced a feedback effect, which decreased the rate of ripening even more (decrease in the slope of the degree of reaction plot during stage III; Fig. 2). The presence of Mg in solution is known to suppress the dissolution and growth of calcium carbonates (e.g., calcite; Chen et al., 2004; Mucci and Morse, 1983; Davis et al., 2000). Thus, is not unexpected that the high concentration of {Mg^{2+}_{aq}] present during stage III significantly reduced the dissolution and reprecipitation process during the Ostwald ripening. Although the aqueous solution was supersaturated with respect to hydromagnesite throughout the reaction, this progressive increase in [Mg^{2+}_{aq}] eventually triggered the nucleation of hydromagnesite at the end of stage III (Fig. 3). Its formation removed [Mg^{2+}_{aq}] from solution (Fig. 7) and induced a dramatic drop in pH following:

$$4Mg^{2+} + 3HCO_3^- + 6H_2O \rightarrow \underset{\text{(hydromagnesite)}}{Mg_4(CO_3)_3(OH)_2 \cdot 4H_2O} + 5H^+ \qquad [5]$$

The main consequence of this Mg removal from the aqueous solution was an acceleration of the monohydrocalcite ripening reaction, which was translated into a rapid growth in particle size and the formation of highly crystalline low-Mg monohydrocalcite.

PHREEQC calculations (Table 1) also revealed that the aqueous solution was in equilibrium or slightly supersaturated with respect to nesquehonite ($Mg(HCO_3)(OH) \cdot 2(H_2O)$) during stages II and II, but became undersaturated in this mineral at stage IV. Nesquehonite was never detected using conventional XRD, synchrotron-based WAXS or HR-TEM imaging. However, Nishiyama et al (2013) suggested that the formation of monohydrocalcite would require the paragenesis of a hydrous Mg-bearing carbonate e.g., nesquehonite, that would transform to hydromagnesite after longer reaction times. Despite the lack of experimental evidences, we can not completely discard the possibility that small amounts of

nanocrystalline nesquehonite were present during stages II and III, and that these eventually transformed to hydromagnesite during stage IV.

The inhibiting effect of Mg has been described previously for other Ca-Mg carbonates (Bischoff, 1968; Berner, 1975; Reddy and Wang, 1980; Mucci and Morse, 1983; Davis et al., 2000). For example, Zhang and Dawe (2000) have suggested that the calcite growth rate is inversely proportional to the Mg concentration in solution. This effect has been attributed to the stronger hydration shell of Mg in comparison to Ca (di Tommaso and de Leeuw, 2010; Moomaw and Maguire, 2008). The higher energy, which Mg needs to dehydrate before incorporating into a carbonate structure controls the kinetics of crystal growth (Mucci and Morse, 1983; Nancollas and Purdie, 1964; De Boer, 1977). Therefore, monohydrocalcite growth would be favoured at lower Mg concentrations.

3.2. Monohydrocalcite chemical and structural variability

The molar fraction of Mg in monohydrocalcite (χ_{MgCO3}) was ~0.25 during stages II and III (i.e., before the formation of hydromagnesite). This is close to the maximum values in the literature for natural or synthetic monohydrocalcites (χ_{MgCO3}= ~0.01-0.34; Brooks et al, 1950; Sapozhnikov and Tsvetkov, 1959; Marschner, 1969; Hull and Turnbull, 1973; Taylor, 1975; Skinner, 1977; Neumann and Epple, 2007; Nebel et al., 2008; Munemoto and Fukushi, 2008; Nishiyama et al., 2013). Many of these studies do not include information about the exact conditions at which monohydrocalcite formed (temperature, solution composition, synthesis method, etc.), therefore the factors controlling χ_{MgCO3} in monohydrocalcite are difficult to evaluate. However, we suggest that the high level of Mg in the monohydrocalcite crystallised from Mg-ACC in this study (Fig. 7) is likely due to the high supersaturation of the initial solution with respect to all carbonate phases.

To test the effect of supersaturation on the incorporation of Mg into the resulting monohydrocalcite, a set of batch experiments were performed at different initial supersaturations (Table 2). Regardless of supersaturation, immediately after mixing the initial solutions an amorphous precursor formed. Experiments with initial SI_{MHC}>2.43 resulted in the crystallization of monohydrocalcite, while only Mg-calcite was obtained at lower supersaturations (Table 2 and Fig. S2). No other Ca/Mg-bearing phases were observed. PXRD analyses of the monohydrocalcite revealed that its crystallite size was inversely proportional to the starting supersaturation (Table 2), varying between 35 nm at SI_{MHC} = 2.43 to 16 nm at SI_{MHC} = 3.89. Furthermore, the χ_{MgCO3} of the monohydrocalcite increased with

498 initial supersaturation, from 0.017 (SI_{MHC} = 2.43) to 0.164 (SI_{MHC} = 3.89, Fig. 9a). This data
499 is consistent with previously published values for χ_{MgCO3} of synthetic monohydrocalcite
500 produced using different initial Mg content in solution and different supersaturations (Fig. 9a;
501 Neumann and Epple (2007); Munemoto and Fukushi (2008), however the original χ_{MgCO3} in
502 the later reference may be higher than reported due to sample treatment). Recently,
503 Nishiyama et al. (2013) synthesized a series of monohydrocalcites using highly variable
504 starting $[Mg^{2+}_{aq}]/[Ca^{2+}_{aq}]/[CO_{3,aq}]$ ratios and most often an excess of carbonate, which lead to
505 a much higher crystallization pH (9.8-11.4) compared to ours (< 9.25). Their data shows that
506 the χ_{MgCO3} in monohydrocalcite is proportional to their starting $[Mg^{2+}_{aq}]/[Ca^{2+}_{aq}]$ ratio, but
507 these is no clear link between supersaturation and Mg contents (χ_{MgCO3}) (Fig. 9a). In addition,
508 Nishiyama et al. (2013) used a different solution mixing approach (addition of the Na_2CO_3
509 solution to the $CaCl_2/MgCl_2$ solution) compared to ours (addition of the $CaCl_2/MgCl_2$
510 solution to the Na_2CO_3 solution). In an earlier study (Rodriguez-Blanco et al., 2012) we
511 showed that, in the pure carbonate system, different mixing approaches lead to different
512 initial synthesis pH, which in turn dramatically affected the crystallization pathway. Taken as
513 a whole, both the initial $[Mg^{2+}_{aq}]/[Ca^{2+}_{aq}]/[CO_{3,aq}]$ ratios (Nishiyama et al., 2013) and initial
514 supersaturation (this study) are key factors in controlling the Mg content of monohydrocalcite
515 (Fig. 9a). This is also consistent with Loste et al. (2003) who showed that in other carbonate
516 systems, precipitation at high supersaturation levels is so rapid that it results in less
517 distinction between Ca and Mg ions. Therefore we infer that the Mg content of the solid is
518 proportional to the initial supersaturation level and the Mg content in the initial amorphous
519 precursor phase.
520 TGA analysis of the monohydrocalcite samples showed that the H_2O content (0.93 –
521 1.03 per formula unit) was similar in all solids and proportional to initial supersaturation.
522 However, the release of structural water during heating was different depending on the molar
523 fraction of Mg (χ_{MgCO3}) (Fig. 9b). In samples with χ_{MgCO3}<0.06 all water was released at low
524 temperature (150-200°C), while in the Mg-rich monohydrocalcite samples (χ_{MgCO3}>0.06) the
525 retention of water was greater, and it was progressively released during heating to T>450 °C.
526 The final weight loss starting at 550 °C was due to carbonate decomposition. The retention of
527 water to higher temperatures in samples with χ_{MgCO3}>0.06 is related to the greater
528 dehydration energy (~20% higher) of Mg^{2+} in comparison to Ca^{2+} (Nancollas and Purdie,
529 1964; Lippmann, 1973; De Boer, 1977). Ca^{2+} and Mg^{2+} ion dehydration temperature ranges
530 have been defined from 100 - 300 °C, and from 300 - 550 °C respectively, as the release of
531 water associated with Mg^{2+} in the monohydrocalcite structure requires a higher temperature

(300-550 °C) compared to water associated with Ca^{2+}. A detailed quantitative analysis of the TGA data (Fig. 9b, inset) shows that the amount of water released at higher temperatures (> 300 °C) is directly proportional to the molar fraction of Mg in the solid.

Photomicrographs of high or low Mg-containing monohydrocalcite, reveals two distinct morphologies and sizes. Monohydrocalcite χ_{MgCO3}>0.06 consists of individual, nanometer-sized crystals that are <35 nm in size (Fig. 9c). In contrast, monohydrocalcite with χ_{MgCO3}<0.06 consists also of nanoparticulate crystallites (<35nm), but these are aggregated to form elongated particles >5 μm in length. The morphology of these low Mg-monohydrocalcites (Fig. 9d) is identical to "type 2" spherulites described by Granasy et al. (2005), who demonstrated that spherulitic growth occurs via growth front nucleation. This mechanism consists of the continuous nucleation of misaligned equivalent structural units on the surface of growing spherulites, and proceeds via unidirectional growth with low angle branching (Fig. 9d). This process is nucleation controlled with very little, if any, growth of the mineral phase. Spherulites occur in many systems (i.e., organic and inorganic), and usually require high levels of supersaturation in order drive the nucleation controlled process (Shtukenberg et al., 2012; Andreassen, 2005; Andreassen et al., 2010; Beck and Andreassen, 2010). These observations are also consistent previous studies who observed monohydrocalcite crystals with spherulitic morphologies (Kimura and Koga, 2011; Neumann and Epple, 2007; Dahl and Buchardt, 2006, Dejehet et al., 1999; Ferguson et al., 1978; Duedall and Buckley, 1971; Nishiyama et al., 2013).

Therefore, taking into account its crystal chemistry, crystallite size, thermal behaviour and morphology, we propose a new categorization for monohydrocalcite:

- High-Mg monohydrocalcite (χ_{MgCO3}>0.06) consists of individual nanometer-sized crystals (<35 nm) (Fig. 9c) with a significant part (6-25%) of its structural H_2O being associated with the Mg ion, therefore displaying a progressive dehydration during heating to >500°C (Fig. 9b). Such high-Mg monohydrocalcites are uncommon in nature, but can be synthesised in the laboratory at high initial supersaturation levels (SI>3.25).

- Low-Mg monohydrocalcite (χ_{MgCO3}<0.06) which forms a "type 2" spherulite morphology. Less than 6% of the structural water in the low-Mg monohydrocalcite is bonded to Mg, so it fully dehydrates at low temperatures (150-200°C). They have the same composition as natural monohydrocalcites reported in the literature, and can be synthesized in the laboratory at lower supersaturation levels (SI<3.25).

These observations indicate that despite their different morphologies (single nanometer sized crystals and low-angle branching spherulites, respectively; Fig. 9c and 9d)

and levels of supersaturations at which they form, high- and low-Mg monohydrocalcite both crystallize via a nucleation-dominated growth process. The difference in particle size and morphology is likely controlled by the aqueous Mg concentration. At high concentrations, Mg poisons the formation of spherulites but still allows direct nucleation in solution, producing the non-aggregated, individual high-Mg monohydrocalcite crystals. At low supersaturations, the Mg concentration is low and monohydrocalcite forms via growth-front nucleation permitting the development of the low angle branching "type 2" spherulites.

Combining the mechanistic results described above with chemical data from our on-line experiment, and data from other studies (Fig. S3) reveals interesting relationships. Firstly, our on-line experiment shows an increase in nanocrystal sizes during the secondary crystallisation of monohydrocalcite, which is coupled with a significant decrease in χ_{MgCO3} (from ~0.26 to ~0.065). This corresponds to the transition from high- to low-Mg monohydrocalcite, suggesting that the former would be metastable and rapidly transforming to the latter, possibly triggered by the removal of Mg from aqueous solution. Secondly, Davis et al. (2000) determined that the solubility of Mg-calcite ($Ca_{1-x}Mg_xCO_3$; x=0-0.20) varies by approximately half an order of magnitude depending on the Mg content of the solid ($K_{sp} = 10^{-8.0}$ - $10^{-8.5}$). A similar behaviour should be expected for monohydrocalcite. The saturation indexes calculated for monohydrocalcite using the available solubility products from Hull and Turnbull (1973) and Krajl and Brečević (1995) are negative and show a difference of ~0.55 (Fig. 8). We suggest that may be due to difference in the Mg contents of the monohydrocalcites used in their respective studies. This hypothesis is supported by the recent findings of Nishiyama et al. (2013), who reported that the solubility of synthetic monohydrocalcite increases with higher Mg/Ca ratios in the solid. They showed that the K_{sp} of monohydrocalcite can reach maximum values of $K_{sp} = 10^{-6.77}$, which is almost one order of magnitude higher than the value of Hull and Turnbull (1973). Furthermore, Nishiyama et al. (2013) also reported an decrease in monohydrocalcite crystallite size (broadening of Bragg peaks in PXRD) with increasing solid Mg/Ca ratios, which again support our interpretation of the transition from high- to low-Mg monohydrocalcite.

Although an in-depth study of the structural changes in monohydrocalcite as a function of Mg content are outside of the scope of this study, the changes in unit cell parameters during crystallisation (Fig. 6) may be better understood when the χ_{MgCO3} of the monohydrocalcite is taken into account. Regardless of Mg content, the unit cell volume remained virtually constant during stages II-III and only decreased slightly during stage IV ($\Delta V \approx -0.2$ Å^3), in parallel with the decrease in monohydrocalcite χ_{MgCO3}. This small decrease

in volume is a consequence of a mirrored change in a-axis and c-axis dimensions, which may be explained by the change in the monohydrocalcite internal structure during the loss of Mg and the transition from the high to low-Mg type (stage III to IV). The structure of monohydrocalcite is less dense and more open than calcite or aragonite (Effenberger, 1981; Neumann and Epple, 2007; Swainson, 2008), therefore it may more easily adapt to a changing Mg content.

4. SUMMARY AND IMPLICATIONS

Results show that under the conditions of our study monohydrocalcite forms via a Mg-rich ACC precursor. The Mg-ACC forms rapidly then transforms to monohydrocalcite via dissolution and reprecipitation, with monohydrocalcite forming via a nucleation-controlled reaction. This crystallization path is consistent with those observed for the formation of vaterite, calcite and dolomite from (Mg-)ACC. The crystalline phase which forms from the (Mg-)ACC is controlled by the magnesium content of the precursor: pure ACC crystallises to vaterite (Bots et al., 2012); 10% Mg-ACC crystallises to calcite (Rodriguez-Blanco et al., 2012); ~ 30% Mg-ACC crystallises to monohydrocalcite (this study and Nishiyama et al., 2013), and 50% Mg-ACC crystallises to protodolomite/dolomite at higher temperatures (Rodriguez-Blanco et al., 2013). The nucleation controlled growth of these phases from ACC is thought to be due to the high solubility of (Mg-)ACC. Any solution in equilibrium with the amorphous phase will be highly supersaturated with respect to the crystalline phase, leading to nucleation controlled growth. This highlights the universal nature of the nucleation-controlled formation during crystallization from ACC.

Our results highlight the importance of Mg in the formation of monohydrocalcite. The mechanisms by which Mg controls phase stability are complex, but are related to 3 key factors. Firstly, the presence of Mg in solution is known to inhibit the formation of vaterite and calcite (Bischoff, 1968; Kitano, 1966; Bischoff and Fyfe, 1968; Berner, 1975; Mucci and Morse, 1983; Deleuze and Brantley, 1997; Chen et al., 2004; Bots et al., 2011). We suggest that the Mg levels in the current study (i.e. Mg/(Mg + Ca) = 0.3) were high enough to inhibit the formation of both calcite and vaterite, and favoured the formation of monohydrocalcite. Secondly, the hydration shell of Mg is more strongly bound than the hydration shell of Ca (di Tommaso and de Leeuw, 2010; Moomaw and Maguire, 2008). The energy required to desolvate Mg is higher than that of Ca, a fact which explains the higher temperature required

634 to crystallize anhydrous Ca-Mg carbonates, e.g. dolomite or magnesite (Christ and Hostetler
635 1970; Lipmann, 1973; Kittrick and Peryea, 1986; Rodriguez-Blanco et al., 2013). The
636 hydrated nature of monohydrocalcite means that full dehydration of Mg is not required before
637 incorporation into the crystal lattice, therefore it will more likely form than the anhydrous
638 calcium carbonate phases. The TGA analysis of the monohydrocalcite samples support this,
639 as it shows increasing water content with Mg (Fig. 9). Thirdly, monohydrocalcite has a high
640 capacity to accommodate Mg within its structure favouring its formation at higher Mg/Ca
641 ratios. Thus although the initial solutions used in our work were more supersaturated with
642 respect to all anhydrous $CaCO_3$ polymorphs, the formation of monohydrocalcite was
643 favoured.
644 We have shown that the crystal chemistry and growth morphology of
645 monohydrocalcite (Stoffers and Fischbeck, 1974; Taylor, 1975; Munemoto and Fukushi,
646 2008) can be controlled by the initial supersaturation of the aqueous solution. We showed
647 that with increasing supersaturation the Mg content in the monohydrocalcite increases up to
648 χ_{MgCO3} = ~ 0.26, similar to the Mg-contents in Mg-calcites reported previously (Lenders et
649 al., 2012; Goldschmidt et al., 1955; Goldschmidt and Graf, 1958). This has led to us defining
650 2 types of monohydrocalcite i.e. high-Mg and low Mg monohydrocalcite, classified
651 according to their Mg content and morphology. All natural monohydrocalcites, which have
652 been analysed to date, are low Mg monohydrocalites (Mg content ~ 0.01 > χ_{MgCO3} < 0.075,
653 Hull and Turnbull, 1973; Taylor, 1975; Fukushi et al., 2011 and references therein). We
654 suggest that the lack of high-Mg monohydrocalcite in natural environment is due to 2 factors.
655 Firstly, for high-Mg monohydrocalcite to form, initial solutions must be extremely highly
656 supersaturated (SI_{MHC} ~ 3.5 - 4; see Table 1 and Table 2). Such extremely high
657 supersaturation levels are difficult to achieve through natural processes. Secondly, our
658 analysis of the monohydrocalcite crystallization pathway shows that high-Mg
659 monohydrocalcite breaks down to low-Mg monohydrocalcite within hours of its formation,
660 therefore high-Mg monohydrocalcite if it forms at all is likely a transient phase. Furthermore,
661 despite monohydrocalcite not being as abundant as calcite and or aragonite in the geological
662 record, it may still have a potential as a palaeoenvironmental indicator (Solotchina et al.,
663 2009). The isotopic composition of the hydration water in natural low-Mg monohydrocalcites
664 may be useful as a $\delta^{18}O$ record of the palaeoenvironmental conditions of the water from
665 which it crystallized. Such an approach has been successfully applied to other hydrated
666 carbonates like ikaite, which is even scarcer in nature and more unstable than
667 monohydrocalcite (Rickaby et al, 2011; Lu et al., 2012).

Nevertheless, our experiments documented a simple methodology to synthesize monohydrocalcite with specific Mg/Ca ratios, specific particle sizes and shapes (i.e., reactive surface), which may have applications in a number of fields. For example, synthetic monohydrocalcite have been reported to have a high sorption capacity for PO_4^{3-} and AsO_4^{3-} (Yagi and Fukushi, 2012; Yagi and Fukushi, 2011; Fukushi et al., 2011). Thus, by producing monohydrocalcite with specific compositions, particle sizes and shapes the effectivity of these remediation materials could be improved.

Finally, the formation of monohydrocalcite and other CaMg carbonates as a consequence of biological activity has been reported in many systems (Lowenstam, 1981; Sánchez-Román et al., 2011). Microorganisms often promote the formation of highly supersaturated microenvironments which facilitate the precipitation of carbonates (e.g., bacterial cells which absorb Ca, Mg or other metallic cations and act as nucleation sites), even when the conditions for supersaturation have not been reached in the surrounding environment (Vasconcelos and Mckenzie, 1997; Párraga et al., 1998). Systems characterized by high initial aqueous Mg/Mg+Ca values (e.g., ≥ 0.3) will lead to the formation of a Mg-rich ACC precursor, which in turn will crystallize to monohydrocalcite. We suggest that this may be the primary crystallization pathway during biomineralization of monohydrocalcite.

It is interesting to note that monohydrocalcite forms at a broad range conditions in the laboratory and natural environment (i.e. a wide range of solution compositions and Mg/Ca ratios) (Nishiyama et al., 2013; Wood, 2012; Fukushi et al., 2011 and references therein). Yet, monohydrocalcite is scarce in nature, a fact that can be explained by (1) its metastability with respect to aragonite and calcite, and (2) the high supersaturation required to form it compared to other calcium carbonates. However, the chemistry of many carbonates formed during biomineralization processes indicates that they have formed from high Mg/Ca ratios seawater solutions (Davis et al., 2000; Ries, 2010; Ries et al, 2008; Ries, 2004; Reeder et al., 1983), and in some cases at high supersaturations (e.g., Señorale-Pose et al., 2008; Hood et al., 2011; Hood and Wallace, 2012). Furthermore, the paragenesis of some mineral deposits which now contain aragonite also include a variety of Ca-Mg-bearing carbonates like dolomite, hydromagnesite or nesquehonite (Fischbeck and Mueller, 1971; Broughton, 1972). Contrary to monohydrocalcite, aragonite does not necessarily require the presence of Mg to form (e.g., Ogino et al., 1987; Sand et al., 2012), but it is well known that Mg and SO_4^{2-} are the key ions responsible for the switch from calcite to aragonite seas (Sandberg, 1983; Bots et al., 2011). During geological timescales the mineralogy of most calcifying organisms was influenced by the Mg/Ca ratio of the oceans in which they evolved (Stanley, 2006; Porter,

2007). For that reason we consider that some aragonite and (Mg)-calcite deposits that are known to have formed at high Mg/Ca ratios (e.g., coralline red algal beds; rhodoliths, Schäfer et al., 2011; ooids, Brehm et al., 2006; Davies et al., 1978; Ferguson et al., 1978 or microbialites, Burne and Moore, 1987) could be secondary in origin and may have originally been a metastable monohydrocalcite intermediate which recrystallized. This secondary crystallization via monohydrocalcite could be the reason why the skeletal mineralogy and chemistry of calcareous organisms that recorded the Mg/Ca ratio of the seawater in which they grow varied so dramatically during the Phanerozoic (Ries, 2004) and this in turn may affect Mg/Ca ratio – based paleoenvironmental reconstructions. This may also explain why some early Cambrian fossils may have preferentially formed low-cost, high-Mg calcite, while later the increasing physiological cost of biomineralization lead to low Mg-calcite skeletons (Wood, 2011). Whether monohydrocalcite played a role in these early biomineralization processes is still an open question, although if monohydrocalcite was an intermediate phase during these biomineralization reactions it may have big implications for seawater chemistry reconstructions and other paleoproxies and would require further study.

5. **ACKNOWLEDGEMENTS**

This study was supported by the Marie Curie EU-FP6 Mineral Nucleation and Growth Kinetics (MIN-GRO) Research and Training Network under contract MRTNCT-2006-035488. The synchrotron work was funded via Diamond Light Source (grant numbers: SM4595 and SM1132) to Liane G. Benning.

6. REFERENCES

Ahmed, I.A.M., Benning, L.G., Kakonyi, G., Sumoondur, A.D., Terrill, N.J., Shaw, S. (2010) Formation of Green Rust Sulfate: A Combined in Situ Time-Resolved X-ray Scattering and Electrochemical Study. Langmuir, **26**, 6593–6603.

Ajikumar, P.K., Wong, L.G., Subramanyam, G., Lakshminarayanan, R., and Valiyaveettil, S. (2005) Synthesis and characterization of monodispersed spheres of amorphous calcium carbonate and calcite spherules. Cryst. Growth Des., **5**, 1129-1134.

736 Andreassen, J.P. (2005) Formation mechanism and morphology in precipitation of vaterite—
737 nano-aggregation or crystal growth? J. Cryst. Growth, **274**, 256–264.
738 Andreassen, J.P., Flaten, E.M, Beck, R., Lewis, A.E. (2010) Investigations of spherulitic
739 growth in industrial crystallization. Chem. Eng. Res. Des. **88**, 1163–1168.
740 Bateman, J. E.; Derbyshire, G. E.; Diakun, G.; Duxbury, D. M.; Fairclough, J. P. A.; Harvey,
741 I.; Helsby, W. I.; Lipp, J. D.; Marsh, A. S.; Salisbury, J.; Sankar, G.; Spill, E. J.;
742 Stephenson, R.; Terrill, N. J., (2007) The HOTWAXS detector. Nuclear Instruments
743 and Methods in Physics Research Section A: Accelerators, Spectrometers, Detectors
744 and Associated Equipment, **580**, 1526-1535.
745 Beck, R. and Andreassen, J.P. (2010) Spherulitic Growth of Calcium Carbonate. Cryst.
746 Growth Des., **10**, 2934–2947.
747 Berner, R.A. (1975) The role of magnesium in the crystal growth of calcite and aragonite
748 from sea water. Geoch. Cosmochim. Ac., **39**, 489-494.
749 Bird, M.I., Chivas, A.R., Radnell, C.J., and Burton, H.R. (1991) Sedimentological and stable-
750 isotope evolution of lakes in the Vestfold Hills, Antarctica. Palaeogeogr. Palaeocl.,
751 **84**, 109-130.
752 Bischoff, J.L. (1968) Catalysis, inhibition, and the calcite-aragonite problem - II. The
753 vaterite-aragonite transformation. Am. J. Sci., **266**, 80-90.
754 Bischoff, J.L. and Fyfe, W.S. (1968) Catalysis, inhibition, and the calcite-aragonite problem:
755 The aragonite-calcite transformation. Am. J. Sci., **266**, 65-79.
756 Bots, P., Benning, L.G., Rickaby, R.E.M., Shaw, S. (2011) The role of SO_4 in the switch
757 from calcite to aragonite seas. Geology, **39**, 331-334.
758 Bots, P., Benning, L.G., Rodriguez-Blanco, J.D., Roncal-Herrero, T., Shaw, W. (2012)
759 Mechanistic Insights into the Crystallization of Amorphous Calcium Carbonate
760 (ACC). Cryst. Growth Des., **12**, 3806−3814.
761 Brehm, U., Krumbein, W.E., Palinska, K.A. (2006) Biomicrospheres Generate Ooids in the
762 Laboratory. Geomicrobiol. J., **23**, 545–550.
763 Brooks, R., Clark, L.M., Thurston, E.F. (1950) Calcium Carbonate and Its Hydrates. Philos.
764 T. Roy. Soc. A, **243**, 145-167.
765 Broughton, P.L. (1972) Monohydrocalcite in Speleothems: An Alternative Interpretation.
766 Contr. Mineral. and Petrol., **36**, 171-174.
767 Burne, R.V. and Moore, L.S. (1987) Microbialites: Organosedimentary Deposits of Benthic
768 Microbial Communities. Palaios, **2**, 241-254.

769 Carlström, D. (1963) A crystallographic study of vertebrate otoliths. Biol. Bull., **125**, 441-
770 462.
771 Cheary, R.W. and Coelho, A. (1992) A fundamental parameters approach to X-Ray line-
772 profile fitting. J. Appl. Cristallogr., **25**, 109-121.
773 Chen, T. Neville, A. and Yuan, M. (2004) Assessing the effect of Mg^{2+} on $CaCO_3$ scale
774 formation-bulk precipitation and surface deposition. J. Cryst. Growth, **275**, 1341-
775 1347.
776 Christ, C.L. and Hostettler, P.B. (1970) Studies in the system MgO-SiO2-CO2-H2O (II): the
777 activity product constant of magnesite. Am. J. Sci., **268**, 439-453.
778 Coelho, A. A. (2006). Topas Academic v4.1
779 Dahl, K. and Buchardt, B. (2006) Monohydrocalcite in the arctic Ikka Fjord, SW Greenland:
780 First reported marine occurrence. J. Sediment. Res., **76**, 460–471.
781 Davies, P.J., Bubela, B., and Ferguson, J. (1978) The formation of ooids. Sedimentology, **25**,
782 703-730.
783 Davis, K.J., Dove, P.M., De Yoreo, J.J. (2000) The Role of Mg^{2+} as an Impurity in Calcite
784 Growth. Science, **290**, 1134-1137.
785 de Boer R. B. (1977) Influence of seed crystals on the precipitation of calcite and aragonite.
786 Am. J. Sci. **277**, 38-60.
787 de Moor, P.; Beelen, T. P. M.; Komanschek, B. U.; Beck, L. W.; Wagner, P.; Davis, M. E.;
788 van Santen, R. A., (1999) Imaging the assembly process of the organic-mediated
789 synthesis of a zeolite. Chem-Eur J., **5**, 2083-2088.
790 de Moor, P.; Beelen, T. P. M.; van Santen, R. A. (1999b) In situ observation of nucleation
791 and crystal growth in zeolite synthesis. A small-angle X-ray scattering investigation
792 on Si-TPA-MFI. J. Phys. Chem. B, **103**, 1639-1650.
793 Dejehet, F., Idrissi, S., and Debuyst, R.J. (1999) Magnesium and occluded water in calcium
794 carbonate monohydrate. Chim. Phys., **96**, 741–753.
795 Deleuze M. and Brantley S. (1997) Inhibition of calcite crystal growth by Mg^{2+} at 100°C and
796 100 bars: Influence of growth regime. Geochim. Cosmochim. Acta, **7**, 1475-1485.
797 Di Tommaso, D., De Leeuw, N. H. (2010). Structure and dynamics of the hydrated
798 magnesium ion and of the solvated magnesium carbonates: insights from first
799 principles simulations. Phys. Chem. Chem. Phys., **12**, 894-901.
800 Duedall, I.W., Buckley, D.E. (1971) Calcium Carbonate Monohydrate in Seawater. Nature
801 Phys. Sci., **234**, 39-40.

802 Effenberger, H. (1981) Kristallstruktur und Infrarot-Absorptionsspektrum von synthetischem
803 Monohydrocalcit, $CaCO_3 \cdot H_2O$. Monatsh. Chem., **112**, 899-909.
804 Ferguson, J., Bubela, B., and Davies, P.J. (1978) Synthesis and possible mechanisms of
805 formation of radial carbonate ooids. Chem. Geol., **22**, 285-308.
806 Fischbeck, R. and Müller, G. (1971) Monohydrocalcite, hydromagnesite, nesquehonite,
807 dolomite, aragonite, and calcite in speleothems of the Fränkische Schweiz, Western
808 Germany. Contrib. Mineral. Petr., **33**, 87-92.
809 Fukushi, K., Munemoto, T., Sakai, M., Yagi, S. (2011) Monohydrocalcite: a promising
810 remediation material for hazardous anions. Sci. Technol. Adv. Mater., **12**, 064702.
811 Garvie, L.A.J. (2003) Decay-induced biomineralization of the saguaro cactus (Carnegiea
812 gigantea). Am Mineral, **88**, 1879-1888.
813 Garvie, L.A.J. (2006) Decay of cacti and carbon cycling. Naturwissenschaften, **93**, 114-118.
814 Goldschmidt, J.R. and Graf, D.L. (1958) Relation between lattice constants and composition
815 of the Ca-Mg carbonates. Am. Mineral., **43**, 84-101.
816 Goldschmidt, J.R., Graf, D.L., Joensuu, O.I. (1955) The occurrence of magnesian calcites in
817 nature. Geoch. Cosmochim. Ac., **7**, 212-230.
818 Goodwin, A.L., Michel, F.M., Phillips, B.L., Keen, D.A., Dove, M.T., and Reeder, R.J.
819 (2010) Nanoporous structure and medium-range order in synthetic amorphous
820 calcium carbonate. Chem. Mater., **22**, 3197-3205.
821 Gránásy, L., Pusztai, T., Tegze, G., Warren, J.A., and Douglas, J.F. (2005) Growth and form
822 of spherulites. Phys. Rev. E., **72**, 011605.
823 Günther, C., Becker, A., Wolf, G., Epple, M. (2005) In vitro Synthesis and Structural
824 Characterization of Amorphous Calcium Carbonate. Z. Anorg. Allg. Chem., **631**,
825 2830-2835.
826 Hood, A.v.S. and Wallace, M.W. (2012) Synsedimentary diagenesis in a Cryogenian reef
827 complex: Ubiquitous marine dolomite precipitation. Sediment. Geol. **255-256**, 56-71.
828 Hood, A.v.S., Wallace, M.W. and Drysdale, R.N. (2011) Neoproterozoic aragonite-dolomite
829 seas? Widespread marine dolomite precipitation in Cryogenian reef complexes.
830 Geology, **9**, 871-874.
831 Hull, H., Turnbull, A. G. (1973). A thermochemical study of monohydrocalcite. Geoch.
832 Cosmochim. Ac., **37**, 685-694.

833 Ihli, J., Bots, P., Kulak, A., Benning, L.G., Meldrum, F.C. (2012) Elucidating Mechanisms of
834 Diffusion-Based Calcium Carbonate Synthesis Leads to Controlled Mesocrystal
835 Formation. Advanced Functional Materials. doi:10.1002/adfm.201201742

836 Ito, T. (1993) The occurrence of monohydrocalcite from calcareous sinter of cold spring of
837 Shiowakka, Asyoro, Hokkaido. J. Mineral. Petrol. Econ. Geol. **88**, 485-491.

838 Johnson, J., G. Anderson, and D. Parkhurst (2000), Database 'thermo.com.V8.R6.230,' Rev.
839 1.11, Lawrence Livermore Natl. Lab., Livermore, Calif.

840 Kamiya, K., Sakka, S., and Terada, K. (1977) Aragonite formation through precipitation of
841 calcium carbonate monohydrate. Mater. Res. Bull., **12**, 1095-1102.

842 Kimura, T. and Koga, N. (2011) Monohydrocalcite in Comparison with Hydrated
843 Amorphous Calcium Carbonate: Precipitation Condition and Thermal Behavior.
844 Cryst. Growth Des., **11**, 3877-3884.

845 Kitano, Y., and Kanamori, N. (1966) Synthesis of magnesian calcite at low temperatures and
846 pressures. Geochem. J., **1**, 1-10.

847 Kittrick, J.A., Peryea, F.J. (1986) Determination of the Gibbs free energy of formation of
848 magnesite by solubility methods. Soil Sci. Soc. Am. J., **50**, 243-247.

849 Kojima, Y., Kawanobe, A., Yasue, T., Arai, Y. (1993) Synthesis of Amorphous Calcium
850 Carbonate and its Crystallization. J. Ceram. Soc. Jpn., **101**, 1145-1152.

851 Kralj D. and Brečević, L. (1995) Dissolution kinetics and solubility of calcium carbonate
852 monohydrate. Colloid. Surface. A, **96**, 287-293.

853 Last, F.M., Last W.M. and Halden N.M. (2010) Carbonate microbialites and hardgrounds
854 from Manito Lake, an alkaline, hypersaline lake in the northern Great Plains of
855 Canada. Sed. Geol., **225**, 34-49.

856 Lenders, J.J.M., Dey, A., Bomans, P.H.H., Spielmann, J., Hendrix, M.M.R.M., de With, G.,
857 Meldrum, F.C., Harder, S., Sommerdijk, N.A.J.M. (2012) High-Magnesian Calcite
858 Mesocrystals: A Coordination Chemistry Approach. J. Am. Chem. Soc., **134**, 1367-
859 1373.

860 Léveillé, R.J., Fyfe, W.S., Longstaffe, F.J. (2000) Geomicrobiology of carbonate-silicate
861 microbialites from Hawaiian basaltic sea caves. Chem. Geol., **169**, 339-355.

862 Lippmann, F. (1973) Sedimentary carbonate minerals. In Mineral, Rocks and Inorganic
863 Materials. Springer-Verlag. Berlin-Heidelberg, New York (eds. W. von Engelhardt, T.
864 Hahn, R. Roy and P. J. Wyllie), 43–96.

865 Loste, E., Wilson, R.M., Seshadric, R., Meldrum, F.C. (2003) The role of magnesium in
866 stabilising amorphous calcium carbonate and controlling calcite morphologies. J.
867 Cryst. Growth, **254**, 206-218.
868 Lowenstam, H.A. (1981) Minerals formed by organisms. Science, **211**, 1126-1131.
869 Lu, A., Rickaby, R.E.M., Kennedy, H., Kennedy, P., Pancost, R.D., Shaw, S., Lennie, A.,
870 Wellner, J., Anderson, J.B. (2012) An ikaite record of late Holocene climate at the
871 Antarctic Peninsula. Earth Planet. Sc. Lett., **325–326**, 108-115.
872 Machala, L., Zboril, R., Gedanken, A., (2007) Amorphous iron (III) oxide – a review. J.
873 Phys. Chem. B, **111**, 4003–4018.
874 Marchal, J.; Tartoni, N.; Nave, C., (2009) Synchrotron applications of pixel and strip
875 detectors at Diamond Light Source. Nuclear Instruments and Methods in Physics
876 Research Section A: Accelerators, Spectrometers, Detectors and Associated
877 Equipment, **604**, 123-126.
878 Marschner, H. (1969) Hydrocalcite ($CaCO_3 \cdot H_2O$) and Nesquehonite ($MgCO_3 \cdot 3H_2O$) in
879 Carbonate Scales. Science, **165**, 1119-1121.
880 Moomaw, A.S. and Maguire, M.E. (2008) The Unique Nature of Mg^{2+} Channels. Physiology
881 (Bethesda), **23**, 275-285.
882 Mucci, A. and Morse, J.W. (1983) The incorporation of Mg^{2+} and Sr^{2+} into calcite
883 overgrowths: Influences of growth rate and solution composition. Geochim.
884 Cosmochim. Acta., **47**, 217-233.
885 Munemoto, T. and Fukushi, K. (2008) Transformation kinetics of monohydrocalcite to
886 aragonite in aqueous solutions. Journal of Mineralogical and Petrological Sciences,
887 **103**, 345-349.
888 Nancollas, G.H., and Purdie, N. (1964) The kinetics of crystal growth. Q. Rev. **18**, 1-20.
889 Nebel, H. and Epple, M. (2008) Continuous Preparation of Calcite, Aragonite and Vaterite,
890 and of Magnesium-Substituted Amorphous Calcium Carbonate (Mg-ACC). Z. Anorg.
891 Allg. Chem., **634**, 1439-1443.
892 Nebel, H., Neumann, M., Mayer, C. and Epple, M. (2008) On the Structure of Amorphous
893 Calcium CarbonateA Detailed Study by Solid-State NMR Spectroscopy. Inorg.
894 Chem., **47**, 7874-7879.
895 Neumann, M. and Epple, M. (2007) Monohydrocalcite and Its Relationship to Hydrated
896 Amorphous Calcium Carbonate in Biominerals. Eur. J. Inorg. Chem., 1953-1957.

897 Nishiyama, R., Munemoto, T., Fukushi, K. (2013) Formation condition of monohydrocalcite
898 from $CaCl_2$–$MgCl_2$–Na_2CO_3 solutions. Geoch. Cosmochim. Ac., **100**, 217-231.
899 Ogino, T., Suzuki, T., Sawada, K. (1987) The formation and transformation mechanism of
900 calcium carbonate in water. Geoch. Cosmochim. Ac., **51**, 2757-2767.
901 Onac, B.P. (2000) Mineralogical studies and uranium-series dating of speleothems from
902 Scărişoara Glacier Cave (Bihor Mountains, Romania). Theoretical and Applied
903 Karstology, **13**, 33-38.
904 Parkhurst, D.L., 1995, User's guide to PHREEQC--A computer program for speciation,
905 reaction-path, advective-transport, and inverse geochemical calculations: U.S.
906 Geological Survey Water-Resources Investigations Report 95-4227, 143 p.
907 Párraga, J., Rivadeneyra, M.A., Delgado, R., Iñiguez, J., Soriano, M., Delgado, G. (1998)
908 Study of biomineral formation by bacteria from soil solution equilibria. React. Funct.
909 Polym., **36**, 265-271.
910 Pitzer, K.S. (1979) Theory--Ion interaction approach. In R.M. Pytkowicz, ed., Activity
911 Coefficients in Electrolyte Solutions, v. 1, CRC Press, Inc., Boca Raton, Florida, p.
912 157-208.
913 Politi, Y., Batchelor, D.R., Zaslansky, P., Chmelka, B.F. Weaver, J.C., Sagi, I.S., Weiner, S.
914 Addadi, L. (2010) Role of Magnesium Ion in the Stabilization of Biogenic
915 Amorphous Calcium Carbonate: A Structure−Function Investigation. Chem. Mater.,
916 **22**, 161-166.
917 Porter, S.M., 2007, Seawater chemistry and early carbonate biomineralization. Science, **316**,
918 1302.
919 Radha, A. V., Forbes, T.Z., Killian, C.E., Gilbert, P.U.P.A., and Navrotsky, A. (2010)
920 Transformation and crystallization energetics of synthetic and biogenic amorphous
921 calcium carbonate. PNAS, **107**, 16438–16443.
922 Radha, A.V., Fernandez-Martinez, A., Hu, Y., Jun, Y.S., Waychunas, G.A., Navrostsky, A.
923 (2012) Energetic and structural studies of amorphous $Ca_{1-x}Mg_xCO_3 \cdot nH_2O$ ($0 \le x \le 1$).
924 Geoch. Cosmochim. Ac., **90**, 83-95.
925 Raz, S., Hamilton, P.C., Wilt, F.H., Weiner, S., Addadi, L. (2003) The Transient Phase of
926 Amorphous Calcium Carbonate in Sea Urchin Larval Spicules: The Involvement of
927 Proteins and Magnesium Ions in Its Formation and Stabilization. Adv. Funct. Mater.,
928 **13**, 480-486.

929 Reeder, R.J. (1983) Carbonates: mineralogy and chemistry. Rev. Mineral. (Ed. Reeder, R.J.)
930 Vol 11. 399 pp. Mineralogical Society of America.
931 Reddy, M.M. and Wang, K K. (1980) Crystallization of calcium carbonate in the presence of
932 metal ions. I. Inhibition by magnesium ion at pH 8.8 and 25°C. J. Cryst. Growth, **50**,
933 470-480.
934 Rickaby, R.E.M., Shaw, S., Bennitt, G., Kennedy, H., Zabel, M., and Lennie, A. (2006)
935 Potential of ikaite to record the evolution of oceanic $\delta^{18}O$. Geology, **34**, 497-500.
936 Ries, J.B. (2004) The effect of ambient Mg/Ca on Mg fractionation in calcareous marine
937 invertebrates: a record of Phanerozoic Mg/Ca in seawater. Geology, 32, 981-984.
938 Ries, J.B. (2010) Review: geological and experimental evidence for secular variation in
939 seawater Mg/Ca (calcite-aragonite seas) and its effects on marine biological
940 calcification. Biogeosciences, **7**, 2795-2849.
941 Ries, J.B., Anderson, M.A., and Hill, R.T. (2008) Seawater Mg/Ca controls polymorph
942 mineralogy of microbial $CaCO_3$: A potential proxy for calcite-aragonite seas in
943 Precambrian time. Geobiology, **6**, 106–119.
944 Rivadeneyra, M.A, Párraga,. J., Delgado, R., Ramos-Cormenzana, A., Delgado, G. (2004)
945 Biomineralization of carbonates by Halobacillus trueperi in solid and liquid media
946 with different salinities. FEMS Microbiol Ecol., **48**, 39-46.
947 Rodriguez-Blanco, J.D. Shaw, S. and Benning, L. G. (2008) How to make 'stable' ACC:
948 protocol and preliminary structural characterization. Mineral. Mag., **72**, 283-286.
949 Rodriguez-Blanco, J.D., Shaw, S. and Benning, L.G. (2011) The kinetics and mechanisms of
950 Amorphous Calcium Carbonate (ACC) crystallization to calcite, via vaterite.
951 Nanoscale, **3**, 265-271.
952 Rodriguez-Blanco, J.D., Shaw, S. Bots, P., Roncal-Herrero, T., and Benning, L.G. (2012)
953 The role of pH and Mg on the stability and crystallization of amorphous calcium
954 carbonate. J. Alloy. Compd., 536, S477-S479.
955 Rodriguez-Blanco, J.D., Shaw, S. and Benning, L.G. (2013) The kinetics and mechanisms of
956 dolomite crystallization. In second revision with Geoch. Cosmochim. Ac.
957 Roncal-Herrero, T., Rodríguez-Blanco, J.D., Benning, L.G., and Oelkers, E.H. (2009)
958 Precipitation of iron and aluminum phosphates directly from aqueous solution as a
959 function of temperature from 50 to 200° C. Cryst. Growth Des., **9**, 5197–5205.

960 Roncal-Herrero, T., Rodríguez-Blanco, J.D., Oelkers, E.H., and Benning, L.G. (2011) The
961 direct precipitation of rhabdophane (REE-PO4.nH2O) from acidic aqueous solutions
962 at 5 to 100 °C. J. Nanopart. Res., **13**, 4049-4062.
963 Sánchez-Román, M, McKenzie, J.A, Rebello Wagener, A.L., Romanek, C.S., Sánchez-
964 Navas, A., Vasconcelos, C. (2011) Experimentally determined biomediated Sr
965 partition coefficient for dolomite: Significance and implication for natural dolomite.
966 Geoch. Cosmochim. Ac., **75**, 887-904.
967 Sand, K.K, Rodriguez-Blanco, J.D., Makovicky, E., Benning, L.G., and Stipp, S.L.S. (2012)
968 Crystallization of $CaCO_3$ in Water–Alcohol Mixtures: Spherulitic Growth, Polymorph
969 Stabilization, and Morphology Change. Cryst. Growth Des., 12, 842-853.
970 Sandberg, P.A. (1983) An oscillating trend in Phanerozoic non-skeletal carbonate
971 mineralogy. Nature, **305**, 19-22.
972 Sapozhnikov, D.G. and Tsvetkov, A.J. (1959) Precipitation of hydrous calcium carbonate on
973 the bottom of Lake Issyk-Kul. Dokl. Akad. Nauk. SSSR, **124**, 402-405.
974 Schäfer, P., Fortunato, H., Bader, B., Liebetrau, V., Bauch, T., Reuijmer, J.G.J. (2011)
975 Growth rates and carbonate production by coralline red algae in upwelling and non-
976 upwelling settings along the Pacific coast of Panama. Palaios, **26**, 420-432.
977 Scherrer, P (1918) Estimation of the size and internal structure of colloidal particles by means
978 of röntgen. Nachr Ges Wiss Götingen, Math-Pys. Kl., **2**, 96-100.
979 Señorale-Pose, M., Chalar, C., Dauphin, Y., Massard, P., Pradel, P., Marín, M. (2008)
980 Monohydrocalcite in calcareous corpuscles of Mesocestoides corti. Exp. Parasitol.,
981 **118**, 54-58.
982 Shtukenberg, A.G., Punin, Y.O., Gunn. E., and Kahr, B. (2012) Spherulites. Chem. Rev., **112**,
983 1805–1838.
984 Skinner, H. C. W., Osbaldiston, G. W., and Wilner, A. N. (1977). Monohydrocalcite in a
985 guinea pig bladder stone, a novel occurrence. Am. Mineral., **62**, 273-277.
986 Solotchina, E.P., Prokopenko, A.A., Kuzmin, M.I., Solotchin, P.A., Zhdanova, A.N. (2009)
987 Climate signals in sediment mineralogy of Lake Baikal and Lake Hovsgol during the
988 LGM-Holocene transition and the 1-Ma carbonate record from the HDP-04 drill core.
989 Quatern. Int., **205**, 38-52.
990 Stanley, S.M. (2006) Influence of seawater chemistry on biomineralization throughout
991 Phanerozoic time: Paleontological and experimental evidence. Palaeogeogr.
992 Palaeocl., **232**, 214–236.

993 Stoffers, P., and Fischbeck, R. (1974) Monohydrocalcite in the sediments of Lake Kivu (East
994 Africa). Sedimentology, **21**, 163-170
995 Svergun, D. (1992) Determination of the regularization parameter in indirect-transform
996 methods using perceptual criteria. J. Appl. Crystallogr., **25**, 495-503.
997 Swainson, I.P. (2008) The structure of monohydrocalcite and the phase composition of the
998 beachrock deposits of Lake Butler and Lake Fellmongery, South Australia. Am.
999 Mineral., **93**, 1014-1018.
1000 Taylor, G.F. (1975) The occurrence of monohydrocalcite in two small lakes in the South-East
1001 of South Australia. Am. Mineral., **60**, 690-697.
1002 Tobler, D.J., Shaw, S., and Benning, L.G. (2009) Quantification of initial steps of nucleation
1003 and growth of silica nanoparticles: An in-situ SAXS and DLS study. Geochim.
1004 Cosmochim. Acta, **73**, 5377–5393.
1005 Vallina, B., Rodriguez-Blanco, J.D., Brown, A.P., Blanco, J.A., Benning, L.G. (2013)
1006 Amorphous dysprosium carbonate: characterization, stability and crystallization
1007 pathways. J. Nanopart. Res., **15**, 1438.
1008 Van Driessche, A.E.S., Benning, L.G., Rodriguez-Blanco, J.D., Ossorio, M., Bots, P., García-
1009 Ruiz, J.M. (2012) The Role and Implications of Bassanite as a Stable Precursor Phase
1010 to Gypsum Precipitation. Science, **336**, 69-72.
1011 Vasconcelos, C., and McKenzie, J.A. (1997) Microbial mediation of modern dolomite
1012 precipitation and diagenesis under anoxic conditions (Lagoa Vermelha, Rio de
1013 Janeiro, Brazil). J. Sediment. Res., **67**, 378-390.
1014 Wagner, C. (1961) Theorie der Alterung von Niederschlägen durch Umlösen (Ostwald-
1015 Reifung). Z. Elektrochem., Ber. Bunsenges. Phys. Chem., **65**, 581–591.
1016 Wang, D., Wallace, A.F., De Yoreo, J.J. Dove, P.M. (2009) Carboxylated molecules regulate
1017 magnesium content of amorphous calcium carbonates during calcification. P. Natl.
1018 Acad. Sci. USA., **106**, 21511-21516.
1019 Wood, C.J. (2012) Amorphous Calcium Carbonate (ACC) a key biomineral precursor and an
1020 environmentally significant nanoparticle: thermal transformation analysis and the
1021 effect of magnesium doping. Unpublished BSc Thesis, University of Leeds.
1022 Wood, R.A. (2011) Paleoecology of the earliest skeletal metazoan communities: Implications
1023 for early biomineralization. Earth-Sci. Rev., **106**, 184–190.
1024 Yagi, S. and Fukushi, K. (2011) Phosphate sorption on monohydrocalcite. J. Miner. Petrol.
1025 Sci., **106**, 109-113.

1026 Yagi, S. and Fukushi, K. (2012) Removal of phosphate from solution by adsorption and
1027 precipitation of calcium phosphate onto monohydrocalcite. J. Colloid Interf. Sci., **384**,
1028 128-136.
1029 Zhang Y. and Dave R. A. (2000) Influence of Mg^{2+} on the kinetics of calcite precipitation
1030 and calcite crystal morphology. Geochim. Cosmochim. Acta, **163**, 129-138.
1031

Figures

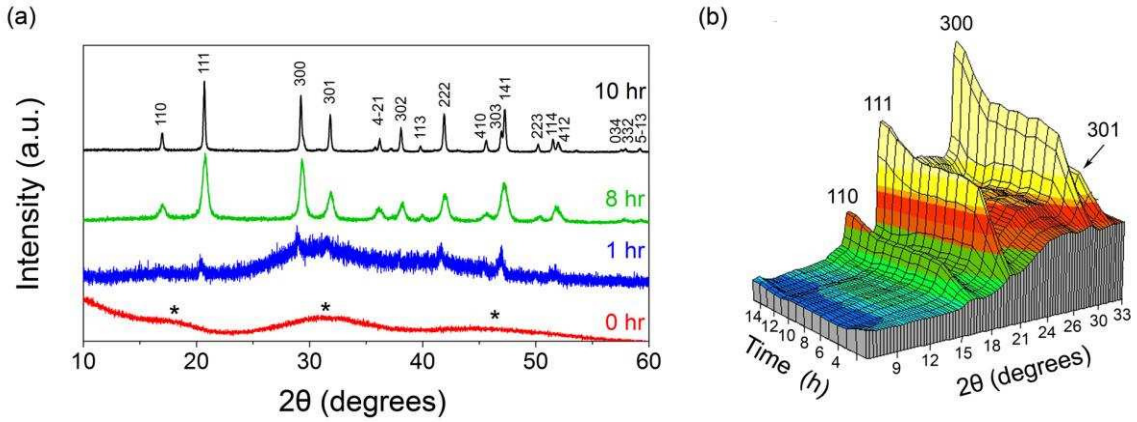

Fig. 1. (a) PXRD patterns from off-line crystallization experiments with samples removed from each run after 0, 1, 8 and 10 hr. (b) 3D WAXS plot showing the time resolved formation of monohydrocalcite from the on-line experiment with only some major peaks shown.

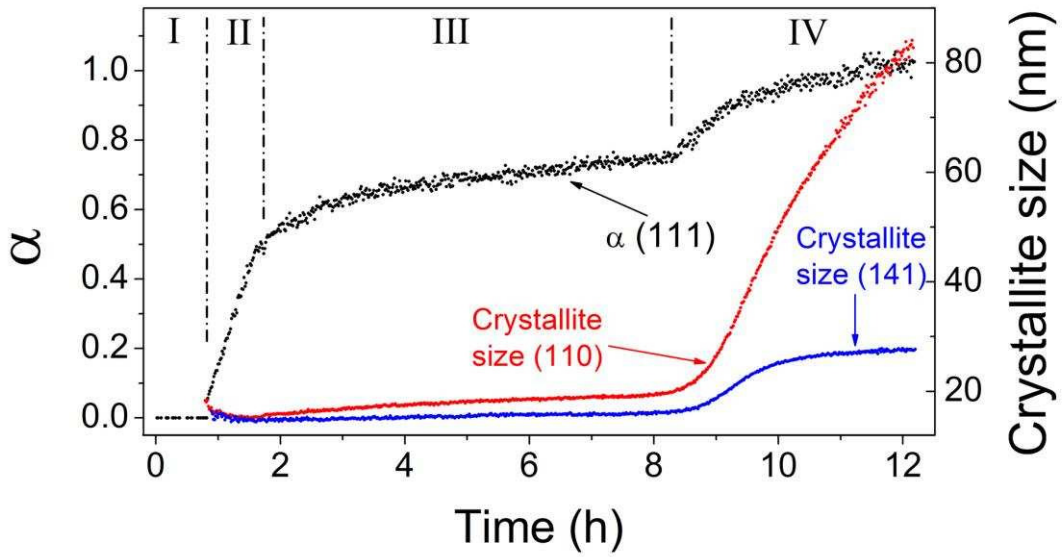

Fig. 2. Evolution of the degree of reaction (α) of the monohydrocalcite (111) Bragg peak (black symbols). The same growth profiles are true for all other Bragg peaks. Shown also with the right-hand y-axis are Scherrer crystallite sizes for the (110) and (141) peaks of monohydrocalcite as a function of time as derived from the WAXS data. I to IV correspond to the crystallization stages described in the text.

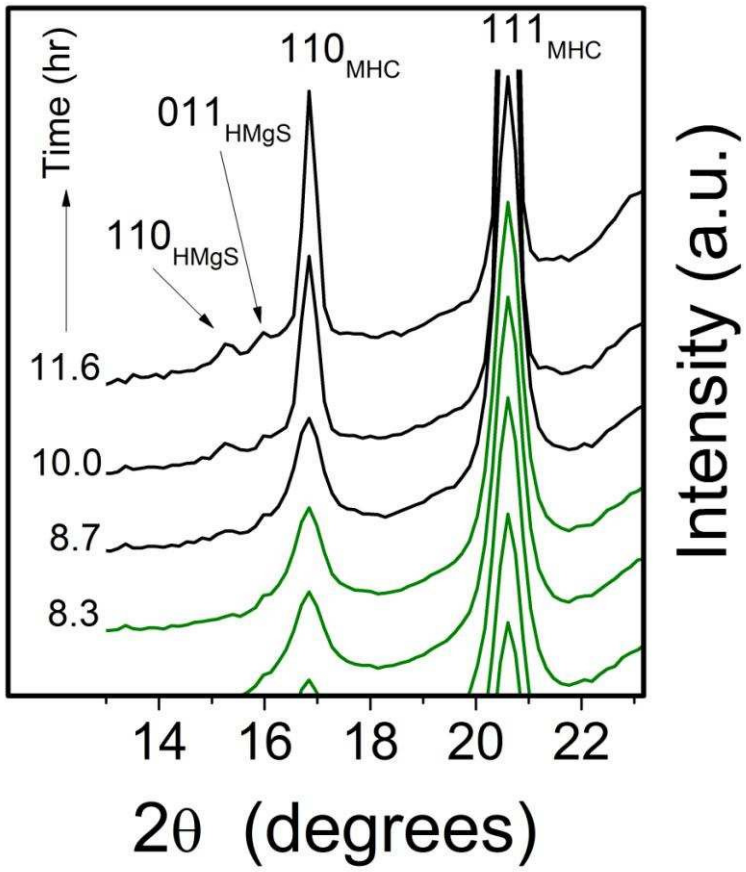

Fig. 3. Selected WAXS patterns from the on-line experiment showing the growth of the monohydrocalcite (MHC) 110 and 111 Bragg peaks and the formation of the small hydromagnesite (HMgS) 110 and 011 Bragg peaks during stages III (green patterns) and IV (black patterns) of the reaction.

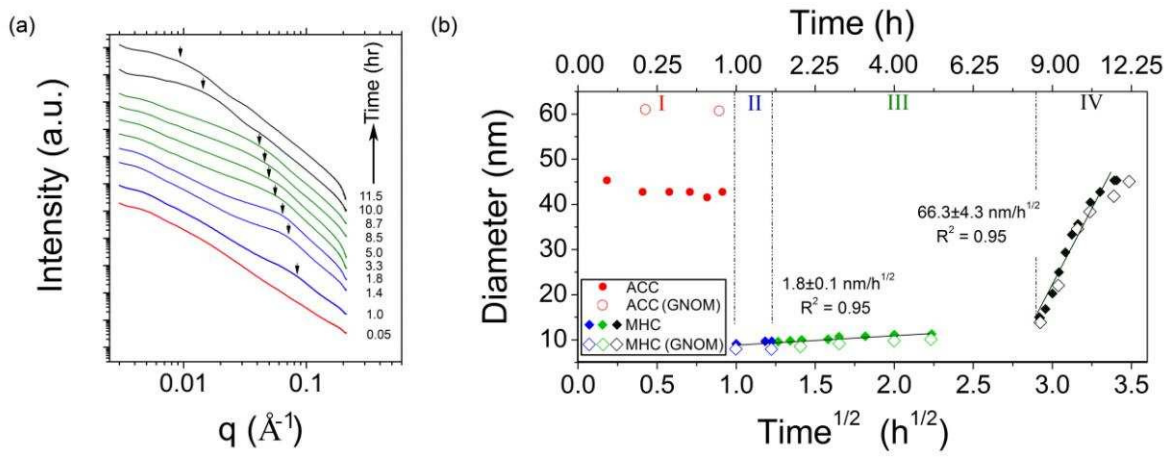

Fig. 4. (a) Double logarithmic plot showing selected SAXS patterns from the on-line in situ experiment with arrows indicating a changing position of the scattering peak, reflecting the growth of monohydrocalcite particles with time; colours of the patterns matches the colour code of the four stages of reaction shown in (b) Time evolution of the particle diameters for the initial amorphous phase (Mg-ACC stage I, red symbols) and for monohydrocalcite (MHC stages II to IV, blue, green and black symbols respectively) as derived from the SAXS data. Empty symbols correspond to GNOM code (Svergun, 1992). The differences in growth rates of the monohydrocalcite particles are evidenced by the fit in stages II-III and IV.

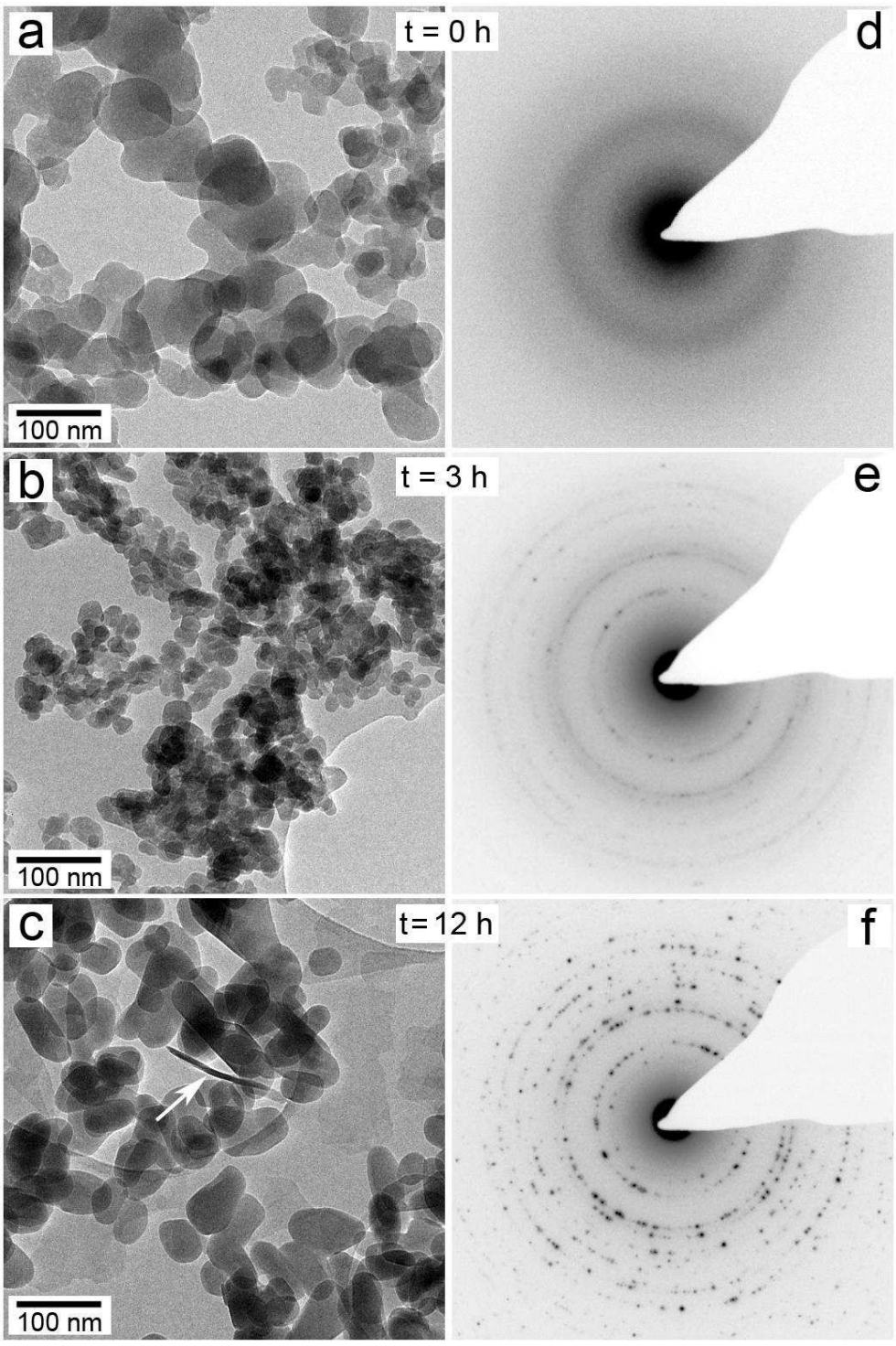

Fig. 5. HR-TEM microphotographs and corresponding SAED patterns of solids during the crystallization reaction. (a, d) Mg-ACC precursor; stage I); (b, e) Monohydrocalcite nanocrystals from stage III; (c, f) Bigger monohydrocalcite particles and a platy hydromagnesite crystal (white arrow) from the end of stage IV.

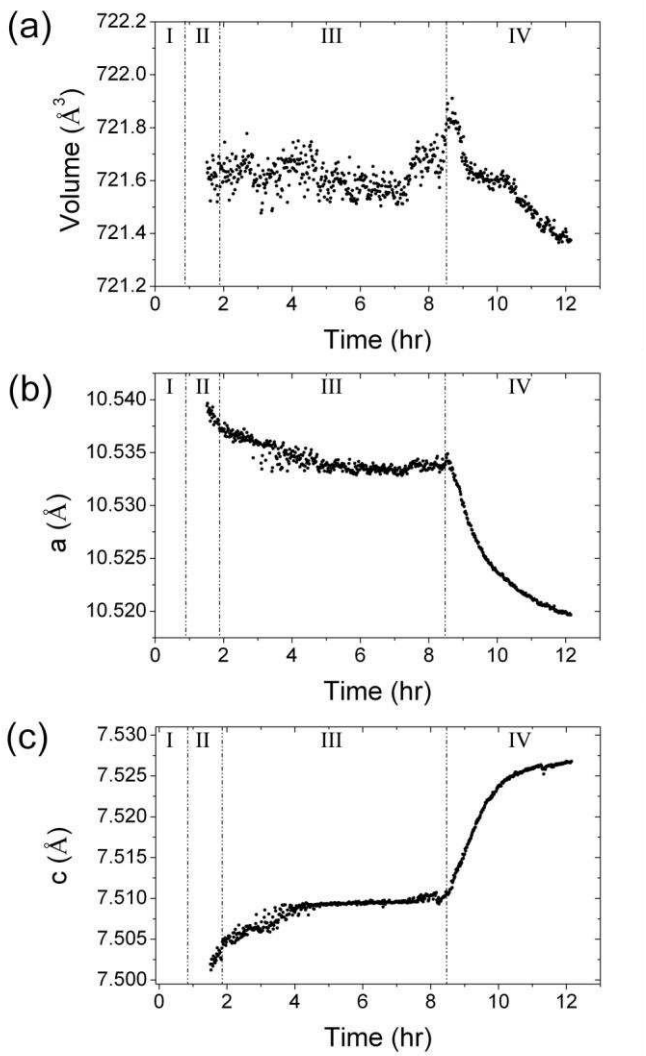

Fig. 6. Evolution of the unit cell volume (a) and of the a and c parameters (panels b and c) for monohydrocalcite over time as derived from the on-line WAXS data for stages II to IV.

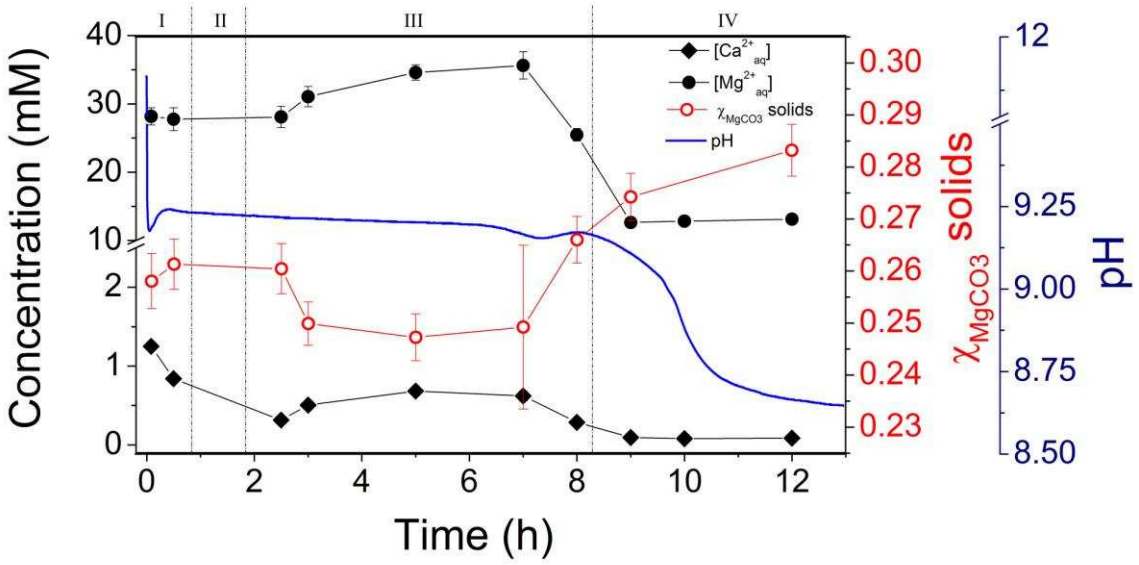

Fig. 7. Evolution of the pH, the concentrations of $[Ca^{2+}_{aq}]$, $[Mg^{2+}_{aq}]$ and of the Mg molar fraction (χ_{MgCO3}) in the solids over the course of the four stages of the crystallization reaction. Error bars correspond to the standard deviation of three measurements each.

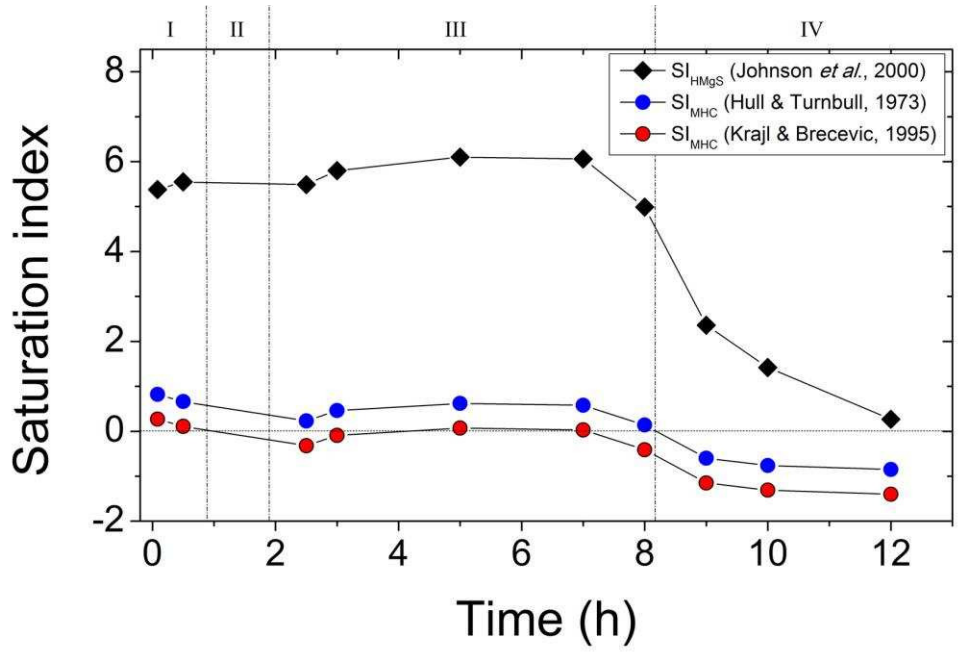

Fig. 8. Evolution of the saturation indexes for monohydrocalcite (SI_{MHC}) and hydromagnesite (SI_{HMgS}) calculated from the data shown in Fig. 7 and Table 1.

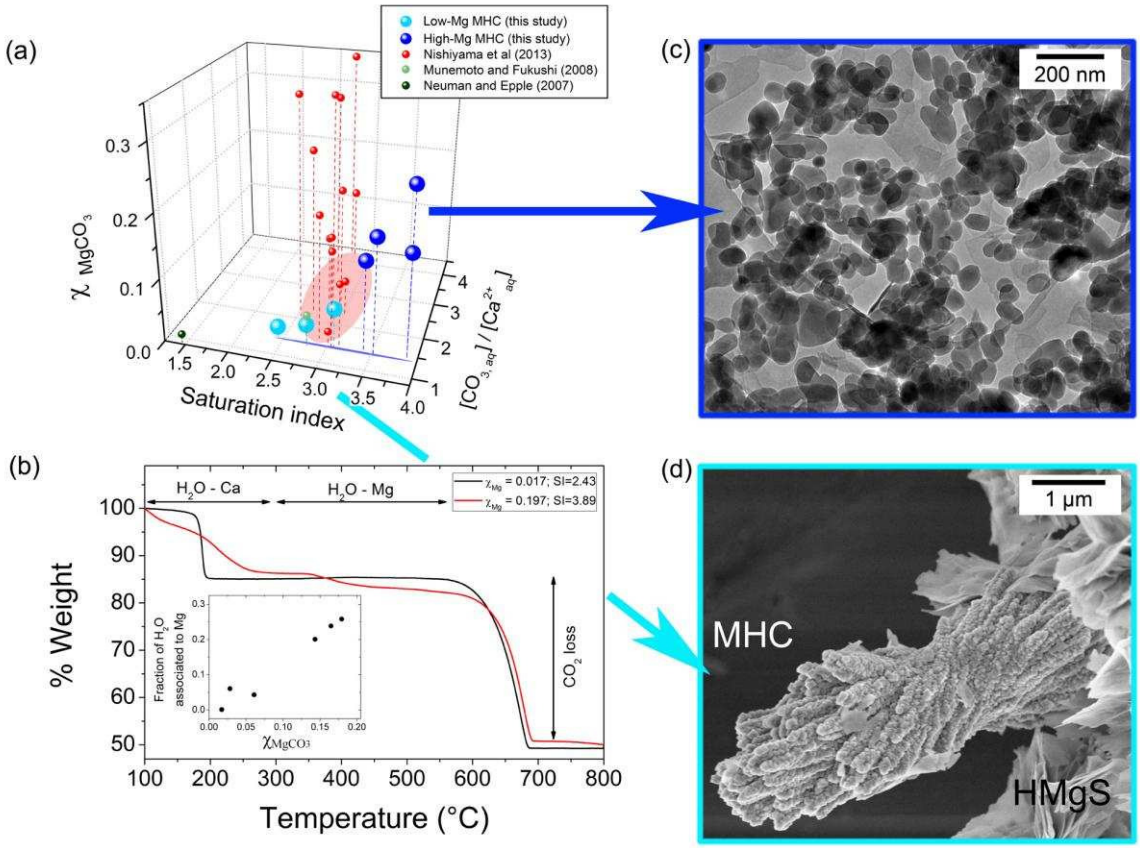

Fig. 9. (a) Three dimensional plot showing the relationship between the molar fraction of Mg (χ_{MgCO3}) in monohydrocalcite as a function of its initial saturation index (SI_{MHC}) and starting $[CO_{3,aq}]/[Ca^{2+}_{aq}]$ ratios. Blue and turquoise larger spheres are our off-line experimental data (Table 2) that were all obtained at the same starting $[CO_{3,aq}]/[Ca^{2+}_{aq}]$ ratio; the smaller, red, green and black spheres correspond to literature data. (b) Comparative TGA graphs for monohydrocalcite synthesised at high (SI=3.89) and low (SI=2.43) initial supersaturations (Table 2) with the inset showing the fraction of Mg-bonded structural water in monohydrocalcite vs. χ_{MgCO3}. Images (c) and (d) illustrate the differences in morphology, particle sizes and formation modes for our high- and low-Mg monohydrocalcite (MHC), respectively. Hydromagnesite (HMgS) crystals are also present in image (d).

Table 1.

Evolution of the aqueous solution composition, the magnesium content in the solids (χ_{MgCO3}) and the solid mineralogy during the course of a typical experiment. Saturation indexes for monohydrocalcite, hydromagnesite and nesquehonite (SI_{MHC} and SI_{HMgS}, SI_{nesq}) were calculated from the measured pH and $[Ca^{2+}_{aq}]$ and $[Mg^{2+}_{aq}]$ values combined with the solubility products for monohydrocalcite reported by (1) Hull and Turnbull (1973), and (2) Krajl and Brečević (1995) and those for hydromagnesite and nesquehonite from Johnson et al. (2000). Average particle sizes were evaluated from the SAXS data or from photomicrographs.

Stage	Time (h)	pH	$[Ca^{2+}_{aq}]$ (mM)	$[Mg^{2+}_{aq}]$ (mM)	χ_{MgCO3} solid	Mineralogy	Particle sizes from SAXS / Crystallite sizes from Scherrer (nm)	Particle sizes from TEM imaging (nm)	SI_{MHC} (1)	SI_{MHC} (2)	SI_{HMgS}	SI_{nesq}
Pre-mixing	0	-	350	150	-	-	40-60 / -		3.89	3.34	13.06	1.17
I	0.083	9.239	1.25 ± 0.05	28.17 ± 1.26	0.258 ± 0.005	Mg-ACC	40-60 / -	~ 40	0.82	0.27	5.38	0.03
	0.5	9.217	0.84 ± 0.04	27.75 ± 1.68	0.261 ± 0.005		43 / -		0.66	0.11	5.55	0.04
II	-	-	-	-	-	-	-	-	-	-	-	-
III	2.5	9.214	0.32 ± 0.02	28.08 ± 1.57	0.260 ± 0.005	MHC	10 / 15	28±7 (L) x 20±5 (W)	0.23	-0.32	5.49	0.04
	3	9.203	0.51 ± 0.03	31.05 ± 1.48	0.250 ± 0.004		11 / 15		0.46	-0.09	5.8	0.11
	5	9.167	0.68 ± 0.03	34.59 ± 1.14	0.247 ± 0.005		11 / 16		0.62	0.07	6.1	0.18
	7	9.171	0.62 ± 0.06	35.62 ± 2.00	0.249 ± 0.016		- / 17		0.58	0.03	6.06	0.19
	8	9.111	0.29 ± 0.01	25.47 ± 0.93	0.266 ± 0.004		- / 17.5		0.14	-0.41	4.99	-0.05
IV	9	8.893	0.09 ± 0.01	12.64 ± 0.75	0.274 ± 0.005	MHC+HMgS	15 / 22.5		-0.6	-1.15	2.36	-0.60
	10	8.646	0.08 ± 0.00	12.83 ± 0.39	-		35 / 37.5	155±80 (L) x 40±30 (W)	-0.76	-1.31	1.42	-0.70
	12	8.609	0.09 ± 0.00	13.12 ± 0.54	0.283 ± 0.005		45 / 45		-0.85	-1.4	0.27	-0.85

Table 2.

Initial stock solution concentrations, and corresponding calculated monohydrocalcite saturation index (SI_{MHC}) for the solution immediately after mixing for each experiment. The first line represents the conditions used in the on-line SAXS/WAXS experiments. The mineralogy, Scherrer crystallite size and Mg (χ_{MgCO3}), and H_2O content of the solid products after 2 h of reaction are also presented.. The saturation index of monohydrocalcite was calculated using the solubility product from Hull and Turnbull (1973).

$Na_2CO_{3(ini)}$ (mM)	$[Ca^{2+}_{aq}]_{(ini)}$ (mM)	$[Mg^{2+}_{aq}]_{(ini)}$ (mM)	SI_{MHC} (t = 0 sec)	Mineralogy from PXRD	Scherrer crystallite size (average) (nm)	χ_{MgCO3}* solid	H_2O content
500	350	150	3.89	MHC	16	0.164	0.99
250	175	75	3.52	MHC	17	0.180	1.03
200	140	60	3.41	MHC	-	0.143	1.00
100	70	30	3.08	MHC	-	0.061	0.97
50	35	15	2.76	MHC	35	0.028	0.95
25	17.5	7.5	2.43	MHC	35	0.017	0.93
12.5	8.75	3.75	2.10	Mg-Calcite	43	0.073	0
5	3.5	1.5	1.63	Mg-Calcite	131	0.032	0

* Errors for χ_{MgCO3} of solids are in all cases lower than 0.002

Fig 1.jpg
Click here to download high resolution image

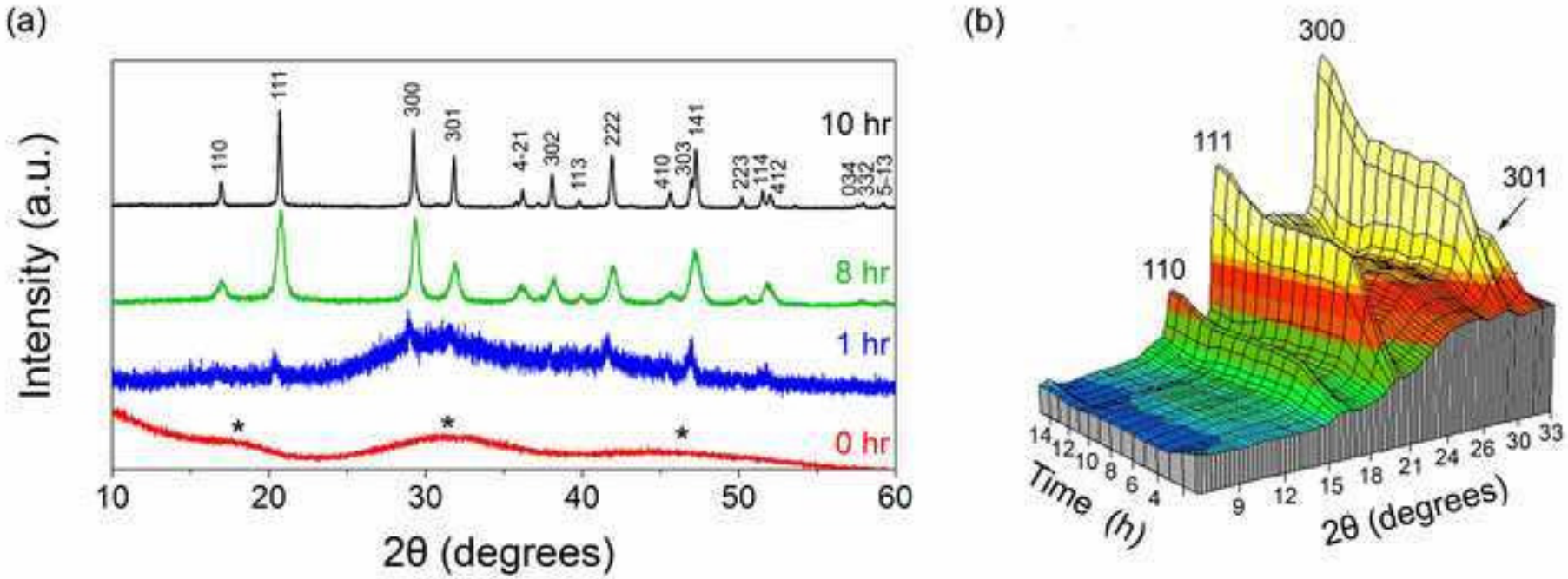

Fig 2.jpg
Click here to download high resolution image

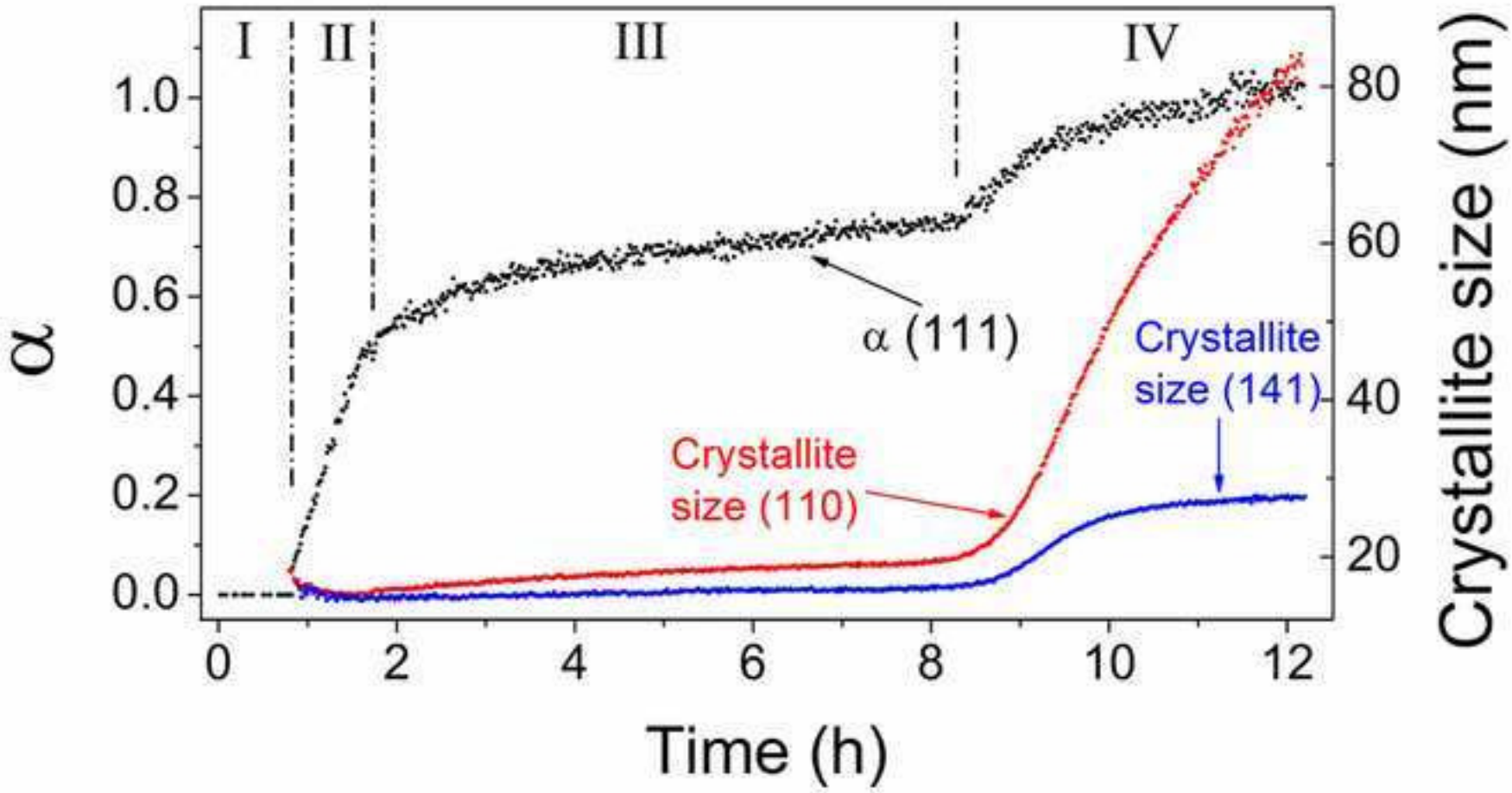

Fig 3.jpg
Click here to download high resolution image

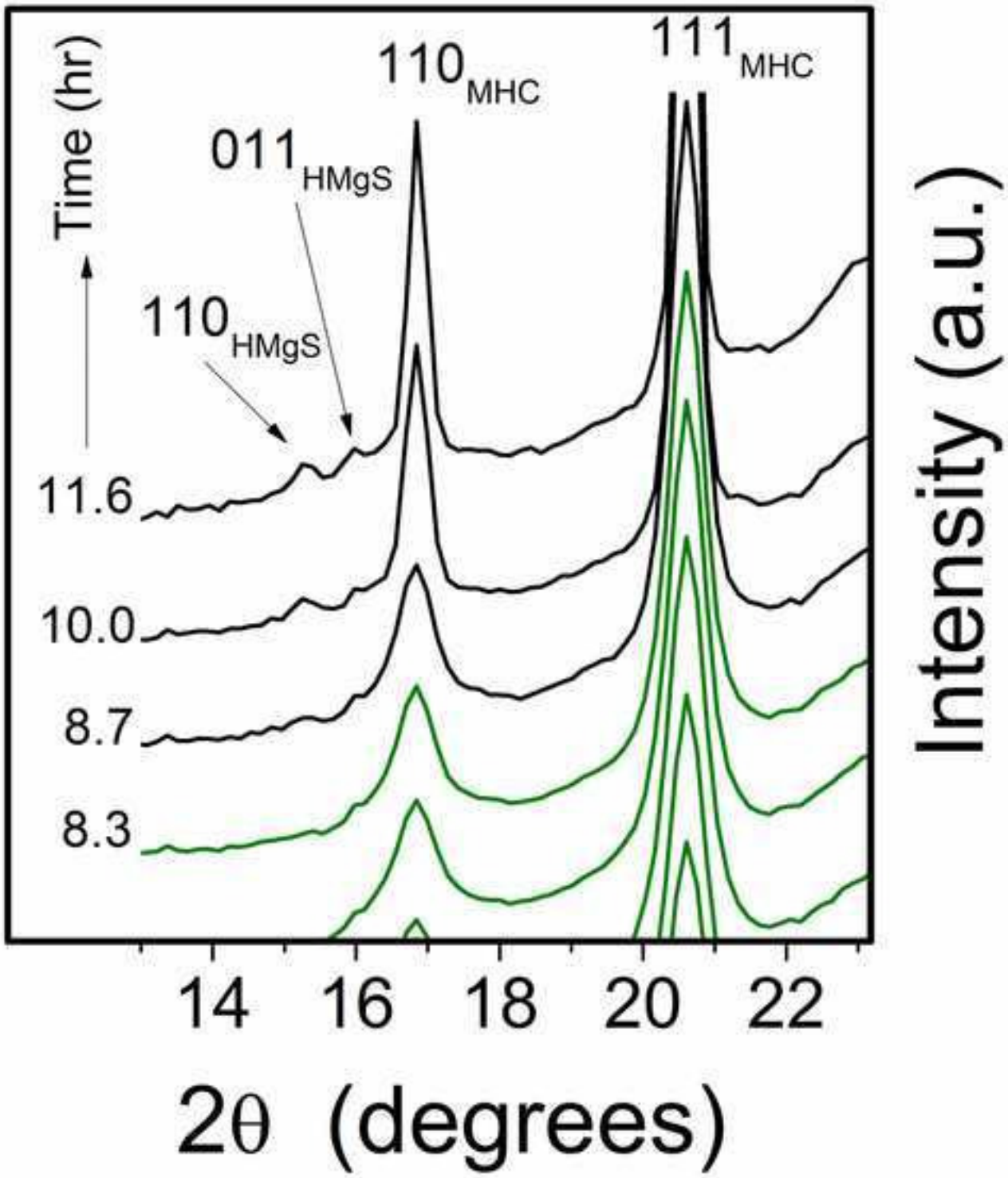

Fig 4.jpg
Click here to download high resolution image

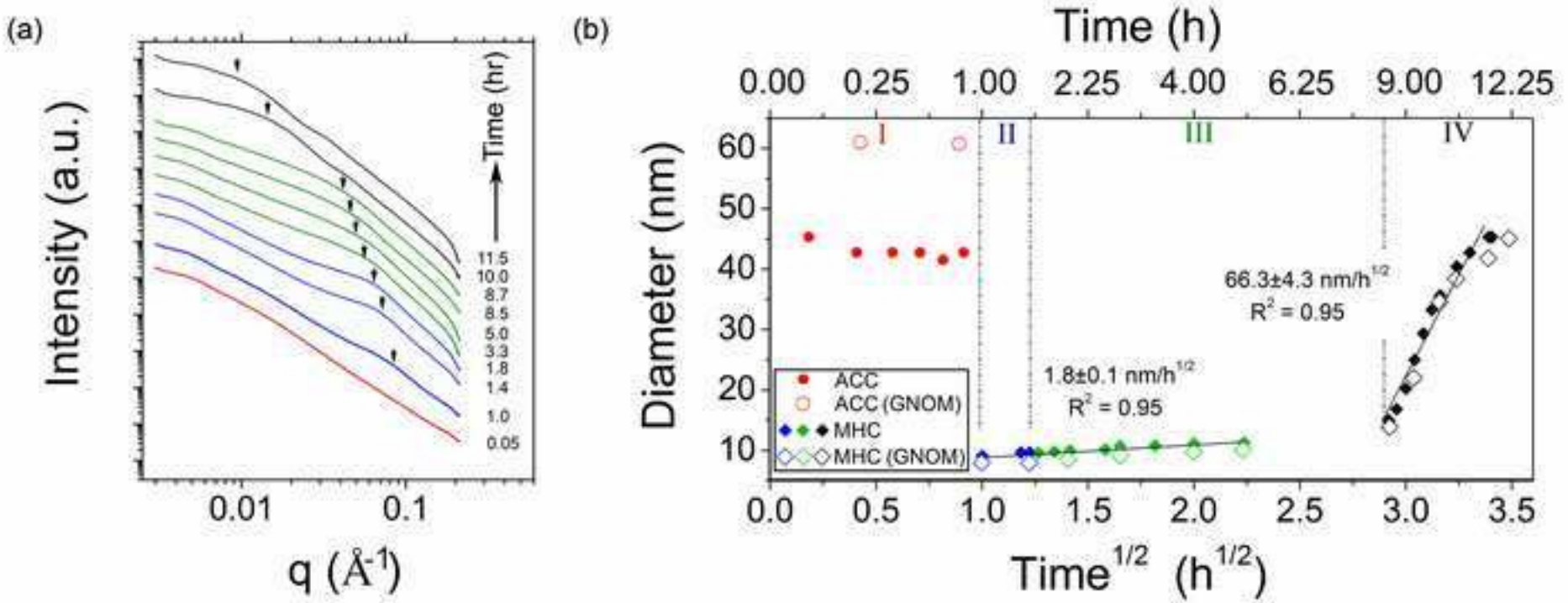

Fig 5.jpg
Click here to download high resolution image

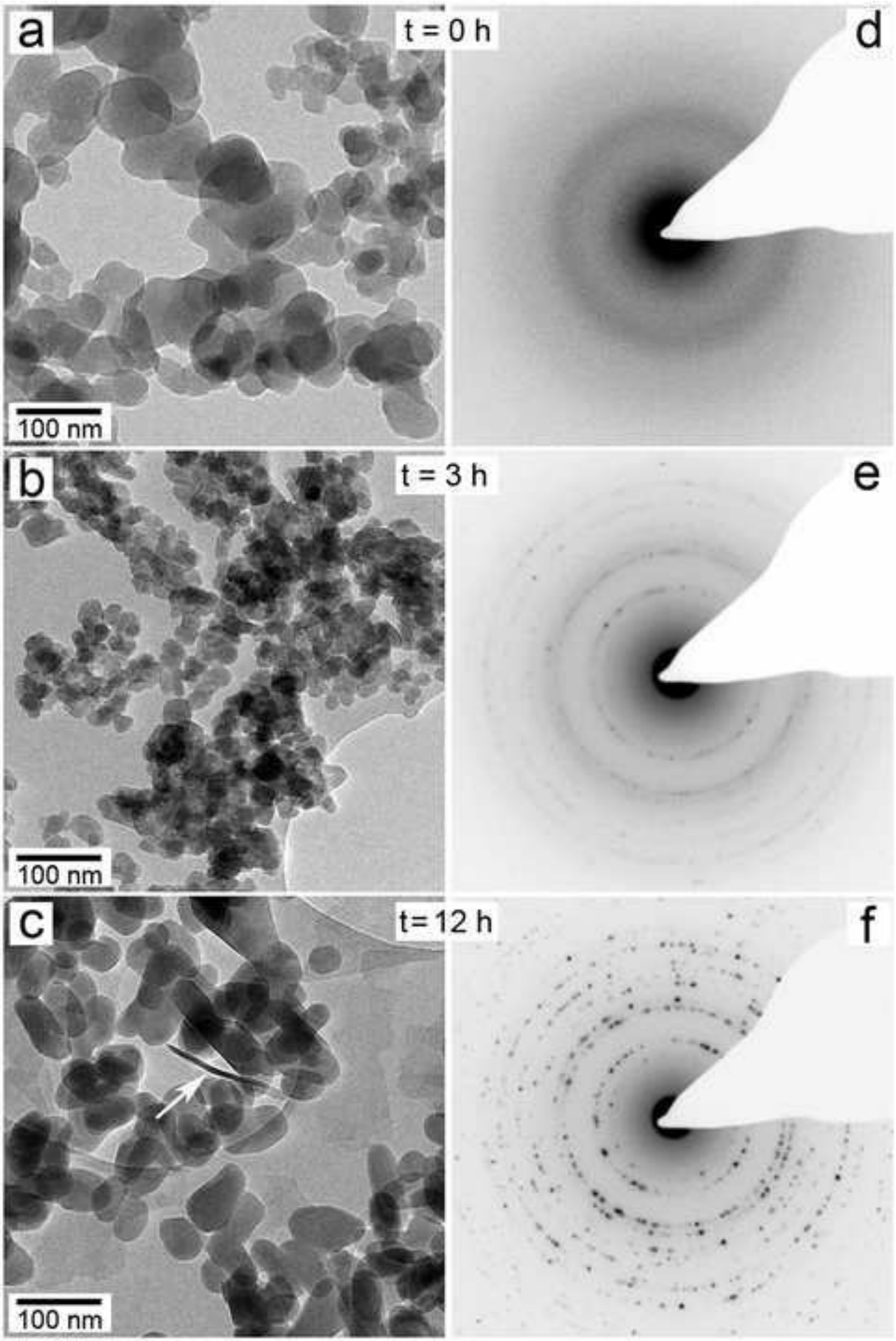

Fig 6.jpg
Click here to download high resolution image

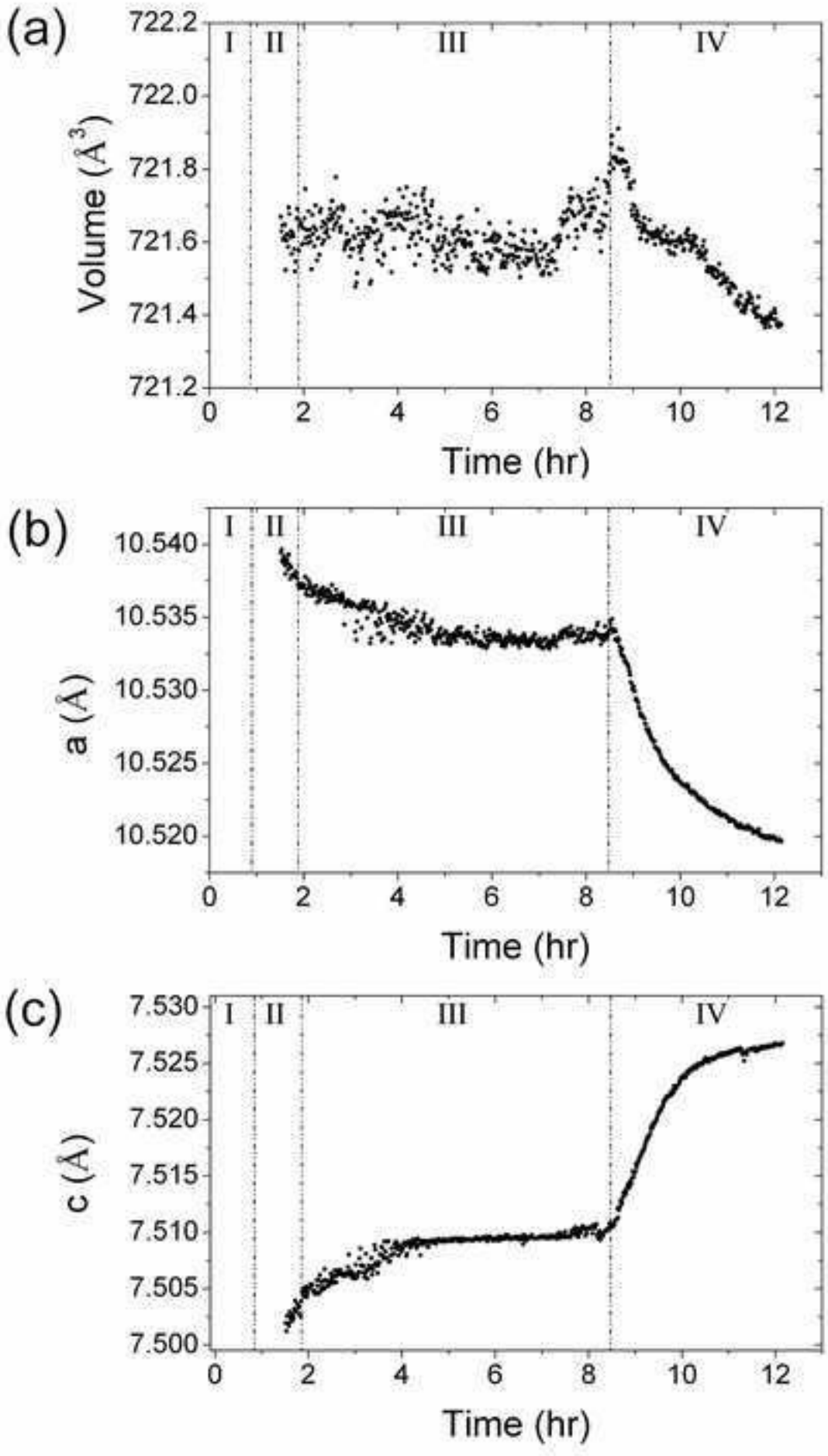

Fig 7.jpg
Click here to download high resolution image

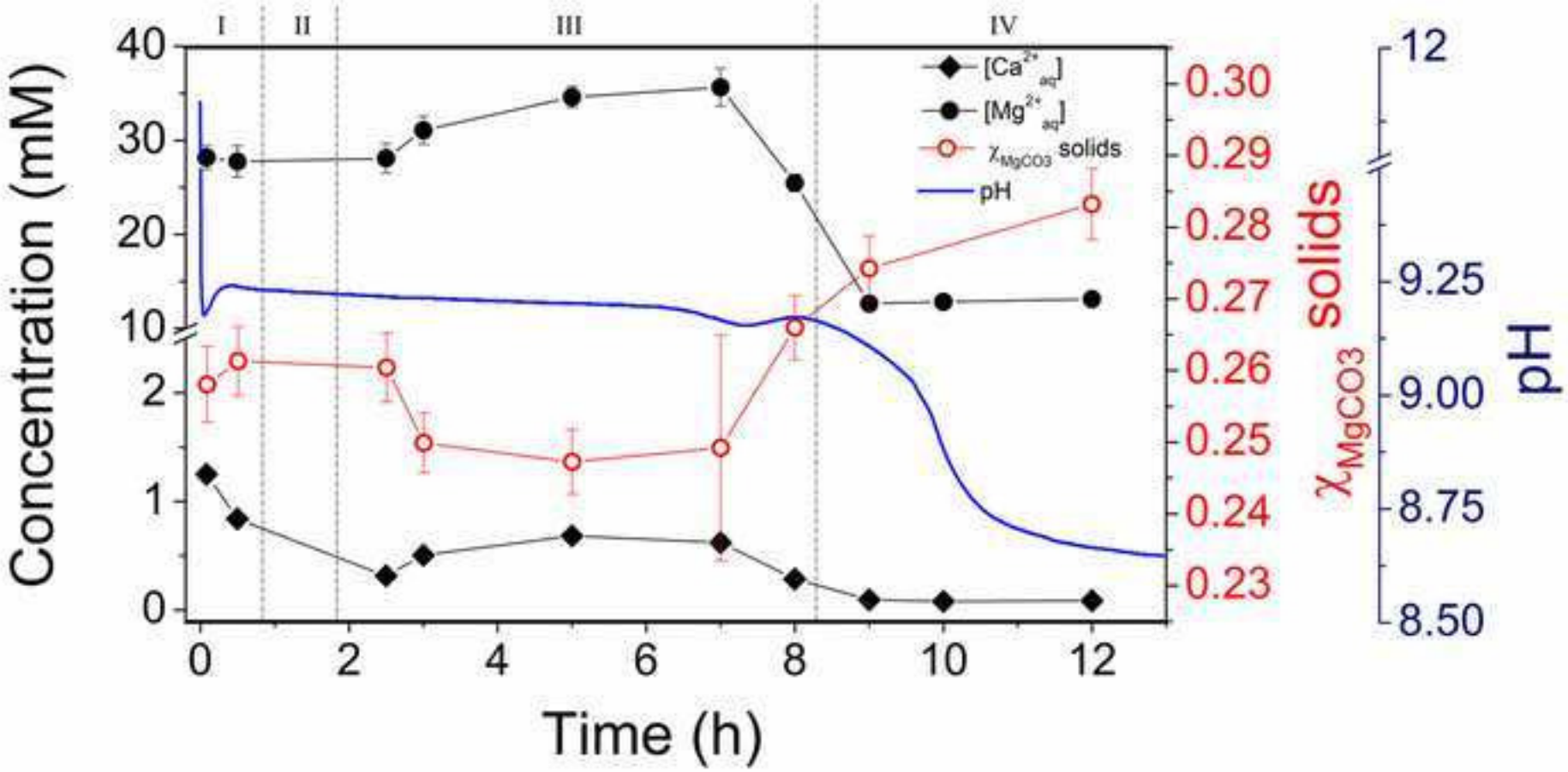

Fig 8.jpg
Click here to download high resolution image

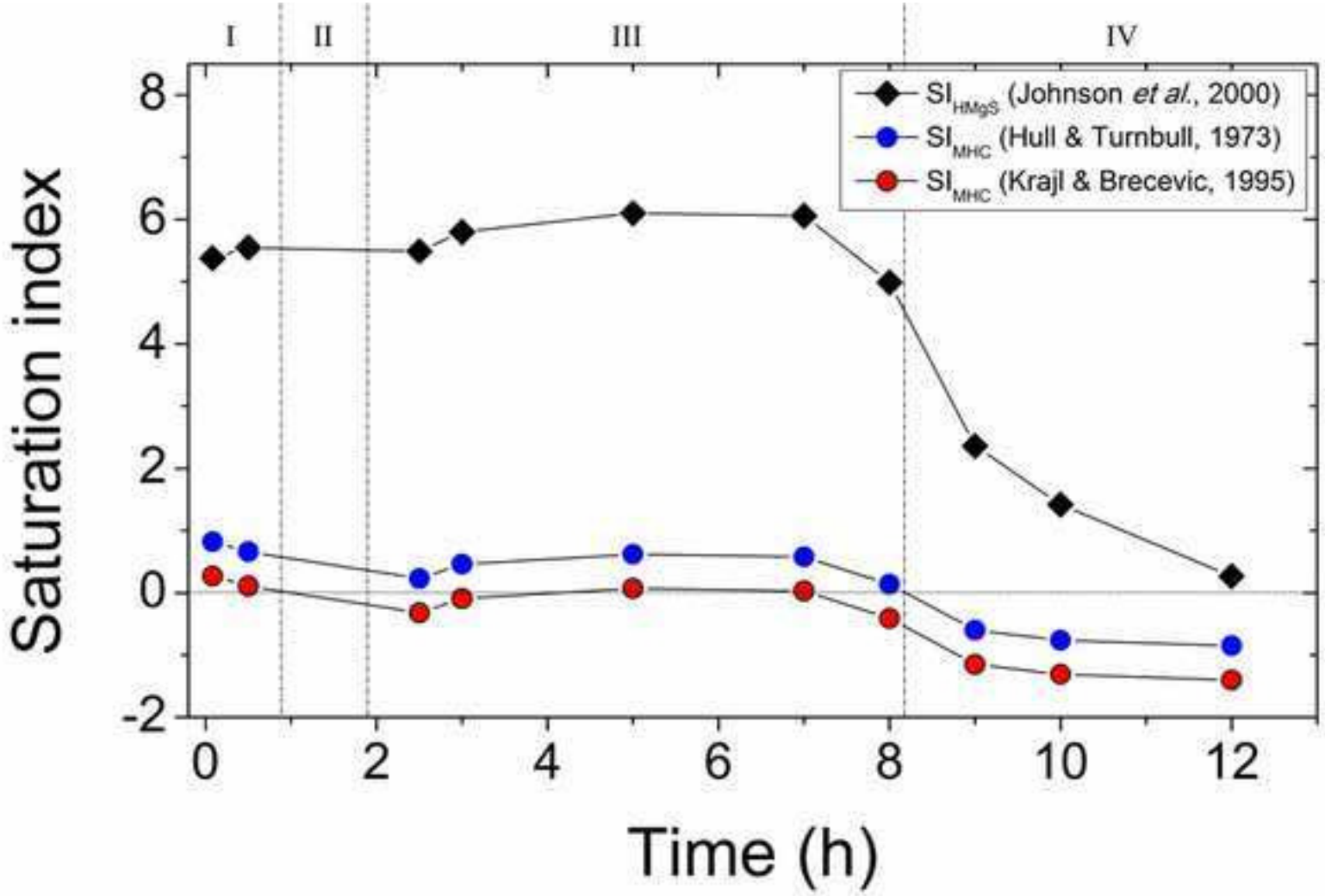

Fig 9.jpg
Click here to download high resolution image

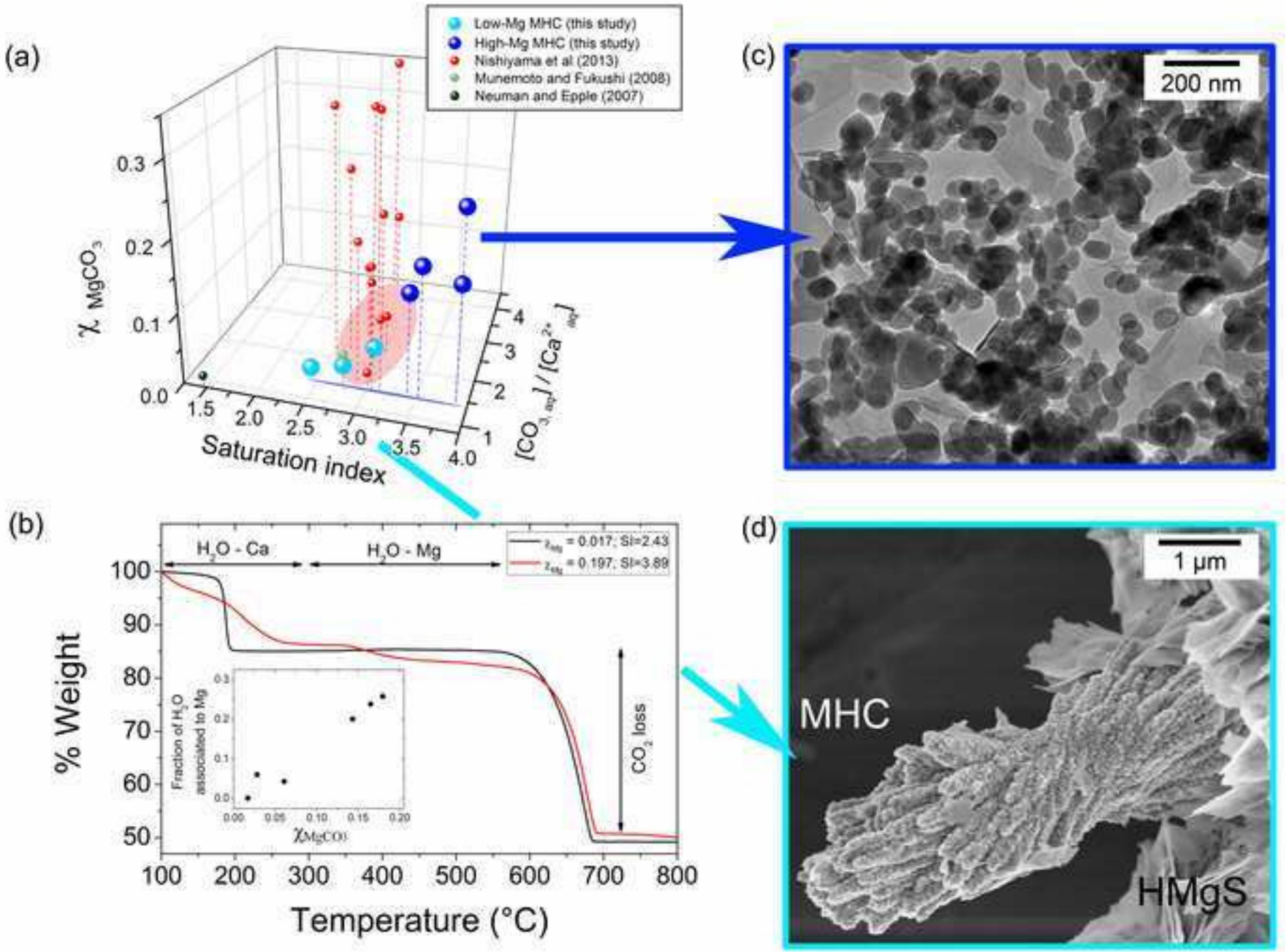

Supplementary Information

Click here to download Electronic Annex: Rodriguez-Blanco, GCA SUPINFO_submission2.docx

Supplementary information

for manuscript:

The role of Mg in the crystallisation of monohydrocalcite.

Juan Diego Rodriguez-Blanco[1,2], Samuel Shaw[1,3], Pieter Bots[1,3], Teresa Roncal-Herrero[1], and Liane G. Benning[1,*]

[1] School of Earth and Environment. University of Leeds. Leeds LS2 9JT. United Kingdom.
[2] Now at the Nano Science Center, University of Copenhagen. 2100 Copenhagen, Denmark.
[3] School of Earth, Atmospheric and Environmental Sciences, The University of Manchester, Oxford Road, Manchester, M13 9PL.
* correspondence: L.G.Benning@leeds.ac.uk

The following diagrams constitute the supplementary information for the manuscript entitled '*The role of Mg in the crystallization of monohydrocalcite*', which details the formation mechanisms for monohydrocalcite from solution via a poorly ordered Mg-rich carbonate precursor.

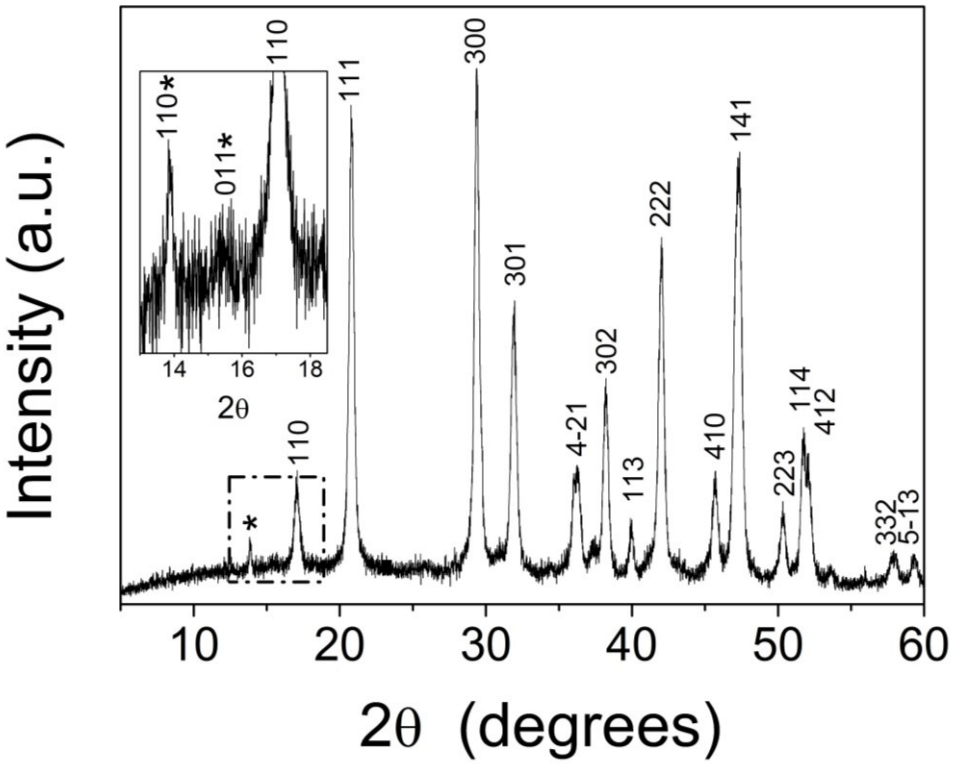

Figure S1: Off-line PXRD pattern of the solids from stage IV; main image shows a pattern of monohydrocalcite with its Bragg peaks marked and with only a tiny peak (at 2 theta of ~ 14; marked with a *) indicating hydromagnesite; in the inset the minor (<5%) contribution from the hydromagnesite with its (110) and (011) Bragg peaks (marked with *) are shown.

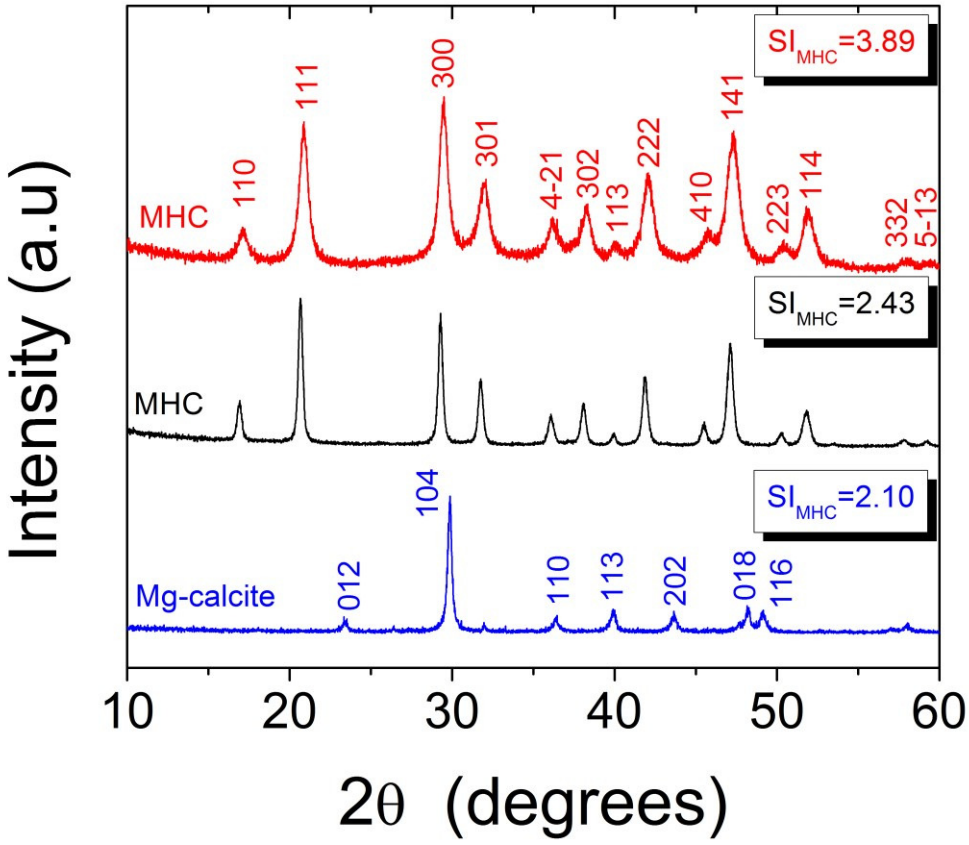

Figure S2: Off-line PXRD patterns of solids obtained after 2 hours at three different initial (prior to mixing) saturation indexes (SI_{MHC}) showing the increase in crystallinity and change in mineralogy from pure monohydrocalcite to Mg-calcite with decreasing initial SI. See Table 2 of manuscript for details.

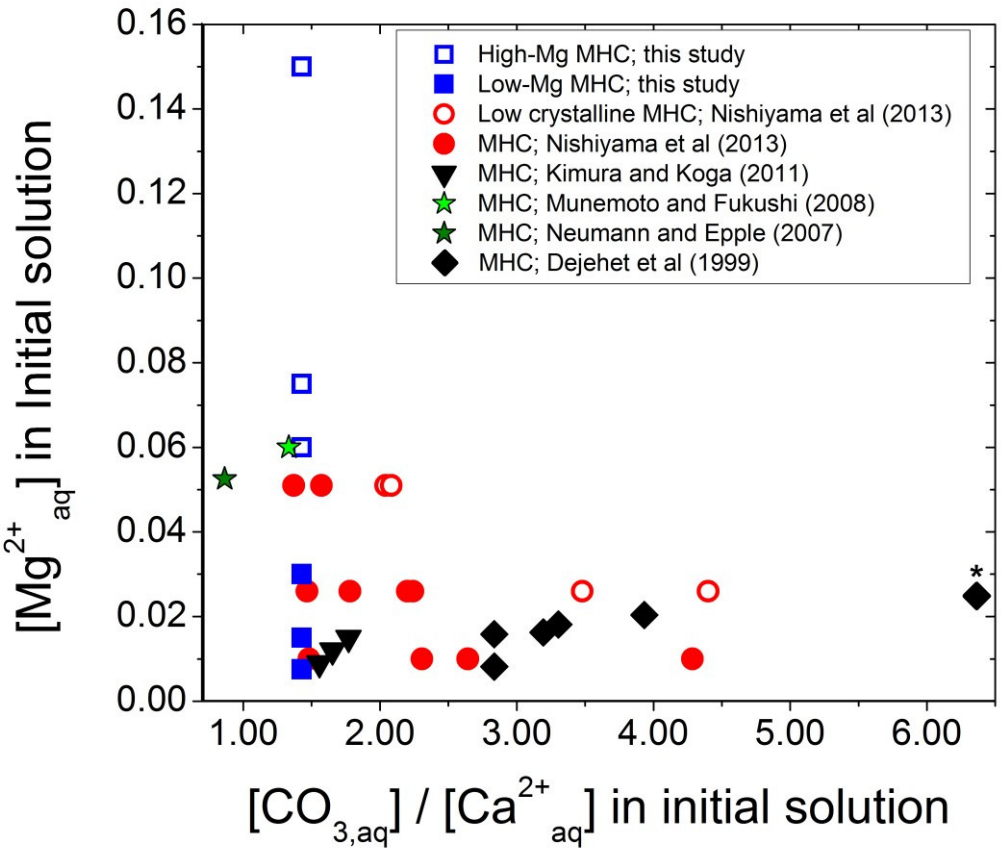

Figure S3: Compositions of monohydrocalcites (MHC) produced in the current study and compared with the literature plotted as a function of initial $[CO_{3,aq}]/[Ca^{2+}{}_{aq}]$ and $[Mg^{2+}{}_{aq}]$ concentrations. Filled and empty blue squares correspond to our low-Mg (χ_{MgCO3}<0.06) and high-Mg (χ_{MgCO3}>0.06) monohydrocalcite samples, respectively. Empty circles correspond to 'low crystalline monohydrocalcite' described by Nishiyama *et al*. (2013), which is structurally and chemically similar to the high-Mg monohydrocalcite described in this study. One of the samples from Dejehet *et al* (1999; marked with an *) has a χ_{MgCO3} equivalent to our high-Mg (χ_{MgCO3}>0.06) monohydrocalcite and was produced at very high initial carbonate concentrations.

References:

Nishiyama, R., Munemoto, T., Fukushi, K. (2013) Formation condition of monohydrocalcite from $CaCl_2$–$MgCl_2$–Na_2CO_3 solutions. *Geochimica et Cosmochimica Acta*, **100**, 217-231.